ESAIM: M2AN 54 (2020) 2125–2157
https://doi.org/10.1051/m2an/2020031

ESAIM: Mathematical Modelling and Numerical Analysis
www.esaim-m2an.org

GEOMETRICALLY INTRINSIC MODELING OF SHALLOW WATER FLOWS

Elena Bachini and Mario Putti*

Abstract. Shallow water models of geophysical flows must be adapted to geometric characteristics in the presence of a general bottom topography with non-negligible slopes and curvatures, such as a mountain landscape. In this paper we derive an intrinsic shallow water model from the Navier–Stokes equations defined on a local reference frame anchored on the bottom surface. The equations resulting are characterized by non-autonomous flux functions and source terms embodying only the geometric information. We show that the proposed model is rotational invariant, admits a conserved energy, is well-balanced, and it is formally a second order approximation of the Navier–Stokes equations with respect to a geometry-based order parameter. We then derive a numerical discretization by means of a first order upwind Godunov finite volume scheme intrinsically defined on the bottom surface. We study convergence properties of the resulting scheme both theoretically and numerically. Simulations on several synthetic test cases are used to validate the theoretical results as well as more experimental properties of the solver. The results show the importance of taking into full consideration the bottom geometry even for relatively mild and slowly varying curvatures.

Mathematics Subject Classification. 76M12, 65M08, 35L65, 58J45.

Received July 8, 2019. Accepted April 25, 2020.

1. Introduction

In many practical applications, such as large-scale ocean modeling [23], river morphodynamics and debris flow [25, 26, 38], avalanche simulation [21], and atmospheric circulation [24], the Shallow Water (SW) approximation is used as an effective tool to derive appropriate reduced models for quantitative simulations of such phenomena. Generally, the typically accepted hypothesis is that the flow develops preferentially along one direction, *e.g.*, horizontal, or, equivalently, that one component of the fluid velocity is negligible with respect to the other two. This is the so-called SW assumption. In most cases, the negligible component of the flow velocity is the one perpendicular to the bottom surface. Then dimensionality reduction proceeds *via* depth integration of the Navier–Stokes (NS) equations to arrive at a two-dimensional system with specific flow rate and water depth as unknowns (see *e.g.*, [14]).

The presence of a curved bottom topography plays an important role, increasing the geometric complexity of the fluid streamlines. It is then difficult to accurately identify the negligible velocity component under the SW hypothesis, as the average flow field drastically departs from a rectilinear behavior. To address this problem, [33, 34] developed a formulation of the SW model in local curvilinear coordinates based on depth

Keywords and phrases. Shallow water, variable topography, intrinsic finite volumes, well balance.

Department of Mathematics "Tullio Levi-Civita", University of Padua, Padua, Italy.
*Corresponding author: putti@math.unipd.it, mario.putti@unipd.it

Article published by EDP Sciences

integration along the normal to the topography. Their approach is valid only for small and essentially one-dimensional bottom curvatures and in practice assumes that the fluid surface is parallel to the bottom. This strategy was extended by [10,11] to consider two-dimensional settings and less restrictive bottom geometries. Starting from the NS equations, the flow velocity component perpendicular to the bottom is considered negligible and a hydrostatic pressure distribution is assumed along local normals. The resulting SW equations are derived by depth integration along the normal direction, under the further hypotheses of a linear velocity distribution (equivalent to assuming constant depth-averaged velocity) and of a fluid depth sufficiently small to guarantee the invertibility of the coordinate transformation. In addition, [10] proved that the resulting SW system (i) admits a conservative energy equation, (ii) preserves the steady-state of a lake-at-rest, and (iii) is an approximation of order ϵ^2, where ϵ is the aspect ratio between the depth of the fluid layer and the characteristic length along which the phenomenon develops (the SW hypothesis states that $\epsilon \ll 1$). Applications of this model are described in [9,19,27,31]. A more intrinsic approach was recently proposed by [18], who suggest to perform depth integration following the so-called "cross-flow" path, along which the tangential component of the fluid velocity is zero. Unfortunately the definition of the "cross-flow" paths is implicit, as it requires the knowledge of the unknown NS velocity field. For this reason, in [18] the authors approximate the "cross-flow" path with the direction normal to the bottom starting from a NS system defined on a curvilinear coordinate reference frame defined on the bottom geometry. The system of SW Equations (SWE) resulting from depth integration turns out to be closely related to the model of [10], and shares similar approximations and limitations in terms of geometry of the bed topography.

In this paper, we propose a new geometrically intrinsic formulation of the SWE on general topography and study its mathematical structure and numerical solution. Our developments take inspiration from the works of [10] and of [18], both of whom include the effects of the bottom geometry on the SW system. In the former, the derived model includes the bottom geometry using a three-dimensional reference system. As a consequence, the SW equations contain non-conservative terms that need to be properly handled. In the latter approach, depth integration proceeds using a local reference system defined on the bottom surface. Again, non-conservative terms arise in the covariant form of the equations. Similarly, in our work we describe the SW model on a local reference frame. However, differently from previous work, by careful use of contravariant and covariant vectors we are able to arrive at a system that is completely intrinsic to the bottom geometry, with a source term that contains only bottom slope and curvature information. The resulting set of equations is characterized by spatially varying flux functions and bottom-related sources. We study the mathematical structure of the proposed approximation, proving order of accuracy with respect to a "geometric" aspect ratio parameter $\epsilon_{\mathcal{G}}$ that includes information on local curvatures and slope of the bottom surface. We then study the hyperbolic structure of the proposed system using bottom-intrinsic differential operators and show that it is invariant under rotational transformations, satisfies the lake-at-rest condition, and admits a conserved energy in absence of bed resistance.

The intrinsic nature of the developed SWE allows the formulation of an Intrinsic Finite Volume (IFV) discretization, with some complications due to the presence of non-autonomous fluxes and space-varying source terms. The work in [32] was among the first to study the numerical solution of a hyperbolic system on a general manifold by means of a FV scheme defined on a quadrilateral grid. However, the discretization of geometric quantities based on the surface fundamental forms by quadrilateral meshes turns out to be non-consistent [28]. For this reason, in this work we use triangular grids to derive a first order Godunov type FV method. Surface interpolation of the geometric quantities and the existence of an intrinsic divergence theorem provide the necessary tools to produce a bottom-intrinsic discretization. We prove that approximated quantities converge over subsequent refinements of the surface mesh with second order with respect to the mesh parameter h, and consequently that the discrete divergence theorem is exact up to second order. Using the rotation invariance of the SW equations, we define a geometrically adapted one-dimensional Riemann problem on the curvilinear triangle edges. The HLL Riemann solver [22] is directly applied in solving the Riemann problem after carefully assigning the left and right states at the triangle edges in the corresponding local reference systems. The same considerations are implemented in the HLLC variant used to address problems with more

general wave patterns. Particular attention is required in order to maintain the well-balance property in the discrete setting. We follow the approach proposed by [5, 8] who introduce a general strategy based on a local hydrostatic reconstruction that ensures well-balance and preserves the non-negativity of the water height. We extend the same idea to our intrinsic setting, obtaining a quadrature rule for the curvilinear source integrals that is consistent with the order of the scheme and is exact in a steady-state configuration.

A number of test cases performed over slowly varying bottom topography are used to show the effectiveness of the numerical approach and to verify the importance of considering the geometric features of the bed topography in the equations. The bottom surfaces are defined by explicit formulas, thus allowing the exact calculation of the metric tensor. The approximation of these quantities starting from real digital elevation maps requires the use of computational geometry tools (see *e.g.*, [29, 30]), which is beyond the scope of this study.

The paper is organized as follows. We first describe in Section 2 the general setting and derive the SWE by depth integration along local normals, and study the mathematical properties of the developed system. Then, in Section 3 we develop our intrinsic FV scheme and describe our implementation of the Riemann solver. Next, we show in Section 4 the numerical results, looking at the accuracy of our approximation of the surface geometry by triangulations and of the overall FV approach in non-flat test cases. Conclusions and future perspectives close our work.

2. Shallow water equations in curvilinear coordinates

Consider the classical incompressible Navier–Stokes equations on an open domain $\Omega \subset \mathbb{R}^3$ as:

$$\nabla \cdot \vec{u} = 0, \tag{2.1a}$$

$$\frac{\partial \vec{u}}{\partial t} + \nabla \cdot (\vec{u} \otimes \vec{u}) = -\frac{1}{\rho} \nabla p + \frac{1}{\rho} \nabla \cdot \mathbb{T} + \vec{g}, \tag{2.1b}$$

where $\vec{u} : \Omega \times [0, T] \to \mathbb{R}^3$ is the fluid velocity, ρ its density, assumed constant, $p : \Omega \times [0, T] \to \mathbb{R}$ is the fluid pressure, $\mathbb{T} : \Omega \to \mathbb{R}^{3\times 3}$ the deviatoric stress tensor, and $\vec{g}$ the gravity acceleration. Note that we have used the product rule of differentiation and the incompressibility condition (2.1a) to write the convective term in conservative form. We assume that the domain boundary $\partial\Omega$ is smooth and formed by the union of the bottom surface ($\mathcal{S}_\mathcal{B}$), the free surface ($\mathcal{S}_\mathcal{F}$), and the lateral surface. Smoothness is detailed by the hypothesis that all these surfaces are regular and can be identified by the graph of some function. Thus, the bottom surface will be given by the graph of the function $\mathcal{B} : U \to \mathbb{R}$, $U \subset \mathbb{R}^2$ open, *i.e.*, in a global (Cartesian) coordinate system x^1, x^2, x^3 (GCS) with x^3 assumed aligned with the action of gravity but in the opposite direction:

$$\mathcal{S}_\mathcal{B} := \left\{ (x^1, x^2, x^3) \in \mathbb{R}^3 \text{ such that } x^3 = \mathcal{B}(x^1, x^2) \right\}.$$

Equivalently, $\mathcal{S}_\mathcal{B}$ can be defined as $F_\mathcal{B}^{-1}(0)$, where $F_\mathcal{B}(x^1, x^2, x^3) := x^3 - \mathcal{B}(x^1, x^2)$. Similarly, the fluid free surface $\hat{\mathcal{F}} : U \times [0, T] \to \mathbb{R}$ can be expressed as:

$$\mathcal{S}_{\hat{\mathcal{F}}} := \left\{ (x^1, x^2, x^3, t) \in \mathbb{R}^3 \times \mathbb{R} \text{ such that } x^3 = \hat{\mathcal{F}}(x^1, x^2, t) \right\} = F_{\hat{\mathcal{F}}}^{-1}(0),$$

where now $F_{\hat{\mathcal{F}}}(x^1, x^2, x^3, t) := x^3 - \hat{\mathcal{F}}(x^1, x^2, t)$ contains also the time dependency. The lateral boundary is fixed and independent of time and does not enter our discussion. Next, we want to move our geometric description to a new coordinate system s^1, s^2, s^3 that locally follows the bottom surface.

2.1. Local curvilinear coordinate system

Following [18] we define a local curvilinear reference system (LCS) positioned on the surface representing the topography of the bottom. All the developments, including depth integration, will be carried out with respect to this local reference system. We would like to describe the motion of a fluid particle using a coordinate system that satisfies the following two main conditions:

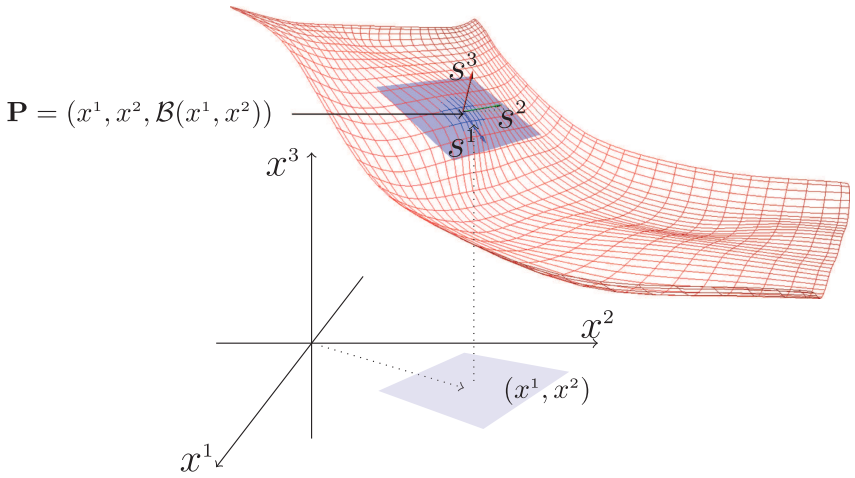

FIGURE 1. Example of bottom surface and LCS coordinates systems.

(i) the first two coordinates run along the bottom surface $\mathcal{S}_\mathcal{B}$, their tangent vectors belonging at each point $\mathbf{P} \in \mathcal{S}_\mathcal{B}$ to the tangent plane $T_\mathbf{P}\mathcal{S}_\mathcal{B}$;
(ii) the third coordinate crosses the surface orthogonally so a vector tangent to $\mathcal{S}_\mathcal{B}$ is everywhere orthogonal to $\mathbf{N}$, the surface normal vector (Fig. 1).

Regarding the ensuing reference frame, the previous requests amount to asking that there exist three vector fields $\mathbf{t}_1, \mathbf{t}_2, \mathbf{t}_3$ in $\mathbb{R}^3$ such that

$$\mathbf{t}_1(\mathbf{P}), \mathbf{t}_2(\mathbf{P}) \in T_\mathbf{P}\mathcal{S}_\mathcal{B} \quad \forall \mathbf{P} \in \mathcal{S}_\mathcal{B},$$

are vector fields in the tangent plane of $\mathcal{S}_\mathcal{B}$ at point $\mathbf{P}$, and $\mathbf{t}_3(\mathbf{P})$ is orthogonal to the other two frame vectors and such that the right-hand rule is satisfied. Moreover, we ask that $\mathbf{t}_1, \mathbf{t}_2, \mathbf{t}_3$ commute in all $\mathbb{R}^3$ and, to ensure numerical stability, be pairwise orthogonal. Because of the regularity of the bottom surface $\mathcal{S}_\mathcal{B}$, given a point $\mathbf{P} \in \mathcal{S}_\mathcal{B}$, there exists a neighborhood $\mathcal{N}_\mathbf{P}$ of $\mathbf{P}$ where we can define a bijective transformation $\Phi_\mathbf{P}$ from the global coordinates x^1, x^2, x^3 to the local coordinates s^1, s^2, s^3. In particular, such a map is a diffeomorphism. Then, given $\mathbf{P} \in \mathbb{R}^3$, we can use the following transformations to express any quantity in both reference systems:

$$\begin{aligned} \Phi_\mathbf{P} : \mathbb{R}^3 &\to \mathbb{R}^3 & \qquad \Psi_\mathbf{P} := \Phi_\mathbf{P}^{-1} : \mathbb{R}^3 &\to \mathbb{R}^3 \\ \mathbf{x}_\mathbf{P} &\mapsto \mathbf{s}_\mathbf{P} & \mathbf{s}_\mathbf{P} &\mapsto \mathbf{x}_\mathbf{P}, \\ \text{GCS} &\to \text{LCS} & \text{LCS} &\to \text{GCS} \end{aligned}$$

where $\mathbf{x}_\mathbf{P} = \left(x^1_\mathbf{P}, x^2_\mathbf{P}, x^3_\mathbf{P}\right)$ and $\mathbf{s}_\mathbf{P} = \left(s^1_\mathbf{P}, s^2_\mathbf{P}, s^3_\mathbf{P}\right)$ are the coordinates of $\mathbf{P}$ with respect to the GCS and the LCS, respectively.

The practical definition of the LCS proceeds as follows. First, we calculate the two tangent vectors $\hat{\mathbf{t}}_1(\mathbf{P})$ and $\hat{\mathbf{t}}_2(\mathbf{P})$ as the differential of $\Phi_\mathbf{P}$ applied to the canonical basis $\mathbf{e}_1, \mathbf{e}_2, \mathbf{e}_3$, of the GCS, or, equivalently, as the derivatives of the coordinate transformation with respect to the LCS variables:

$$\hat{\mathbf{t}}_i(\mathbf{P}) = \mathrm{d}\Phi_\mathbf{P}(\mathbf{e}_i) = \left(\frac{\partial x^1}{\partial s^i}, \frac{\partial x^2}{\partial s^i}, \frac{\partial x^3}{\partial s^i}\right), \quad i = 1, 2,$$

where $\mathrm{d}\Phi_\mathbf{P}$ is the Jacobian matrix of the coordinate transformation. For a regular surface, these two tangent vectors are guaranteed to exist and be linearly independent, their direction depending on the curvature of the bottom surface at $\mathbf{P}$ [1]. Then, vector $\hat{\mathbf{t}}_2$ is orthogonalized with respect to $\hat{\mathbf{t}}_1$ *via* Gram–Schmidt, yielding the

desired orthogonal frame $\mathbf{t}_1, \mathbf{t}_2$ on $T_{\mathbf{P}}\mathcal{S}_{\mathcal{B}}$. The frame-completing vector $\mathbf{t}_3$ is chosen to be orthogonal to the previous two and unitary, *i.e.*, $\|\mathbf{t}_3(\mathbf{P})\| = 1$. Note that normalization of the other two basis vectors cannot be done, as this would amount to assume a zero curvature of $\mathcal{S}_{\mathcal{B}}$ at $\mathbf{P}$, loosing all the geometric information we would like to preserve in our LCS. The associated metric tensor, as a consequence of the orthogonality property, becomes the diagonal matrix given by:

$$\mathcal{G} := \begin{pmatrix} \|\mathbf{t}_1(\mathbf{P})\|^2 & 0 & 0 \\ 0 & \|\mathbf{t}_2(\mathbf{P})\|^2 & 0 \\ 0 & 0 & \|\mathbf{t}_3(\mathbf{P})\|^2 \end{pmatrix} = \begin{pmatrix} h_{(1)}^2 & 0 & 0 \\ 0 & h_{(2)}^2 & 0 \\ 0 & 0 & 1 \end{pmatrix}. \tag{2.2}$$

As a particular case, we use a global parametrization based on the height function (the so-called Monge parametrization). Denoting with $\mathcal{B}_{s^i} = \partial\mathcal{B}/\partial s^i$ the expression of the LCS frame vectors at $\mathbf{P} \in \mathcal{S}_{\mathcal{B}}$ is:

$$\mathbf{t}_1(\mathbf{P}) = [1; 0; \mathcal{B}_{s^1}], \tag{2.3a}$$

$$\mathbf{t}_2(\mathbf{P}) = \left[-\frac{\mathcal{B}_{s^1}\mathcal{B}_{s^2}}{1+(\mathcal{B}_{s^1})^2}; 1; \frac{\mathcal{B}_{s^2}}{1+(\mathcal{B}_{s^1})^2}\right], \tag{2.3b}$$

$$\mathbf{t}_3(\mathbf{P}) = \mathbf{N}(\mathbf{P}) = \frac{\mathbf{t}_1(\mathbf{P}) \wedge \mathbf{t}_2(\mathbf{P})}{\|\mathbf{t}_1(\mathbf{P})\| \, \|\mathbf{t}_2(\mathbf{P})\|} = \frac{[-\mathcal{B}_{s^1}; -\mathcal{B}_{s^2}; 1]}{\|\mathbf{t}_1(\mathbf{P})\| \, \|\mathbf{t}_2(\mathbf{P})\|}. \tag{2.3c}$$

It is important to underline that this particular definition of the tangent vectors has been made for our convenience, but any local coordinate system that satisfies (i) and (ii) can be used. What follows is independent on the parametrization of the surface and the definition of the LCS.

Remark 2.1. To simplify the exposition, we do not fully employ the classical tensor calculus notation and do not use Einstein summation convention. However we need to distinguish physical, covariant, and contravariant versions of vectors and tensors, to ensure coordinate invariance. Consider a basis of $\mathbb{R}^3$ formed by of unit vectors $\mathbf{e}_i$, $i = 1, 2, 3$. For every $\vec{u} \in \mathbb{R}^3$ there is a unique set of coefficients, $u_{(i)}$, such that

$$\vec{u} = \sum_i u_{(i)} \mathbf{e}_i.$$

The values $u_{(i)}$ are called the physical components of $\vec{u}$ relative to the standard basis set, and we denote them by subscripts surrounded with parentheses. In the LCS s^1, s^2, s^3, equipped with the associated metric $\mathcal{G}$ and the reference basis vectors $\mathbf{t}_i$, the physical vector components need to be scaled with $\sqrt{\mathcal{G}}$, or $\sqrt{g_{ii}} = h_{(i)}$. Hence, a vector field $\vec{u}$ can be written as $\vec{u} = \sum_i u^i \mathbf{t}_i$, where the components u^i are called "contravariant" components and are related to the physical components by the relation:

$$u_{(i)} = h_{(i)} u^i.$$

Following standard notation, contravariant components are identified by means of superscripts. Note that the LCS basis $\mathbf{t}_i$ is formed by "covariant" vectors, and we use subscripts for their identification.

Next, we need to adapt to the LCS the expressions of the differential operators that appear in the Navier–Stokes equations, *i.e.*, the gradient of a scalar function, the divergence of a vector field, and the divergence of a tensor field, as stated in the following lemma, which we report without proof.

Lemma 2.2. *Let (s^1, s^2, s^3) be the coordinate set of the LCS and $\mathcal{G} = \left\{g_{ii} = h_{(i)}^2\right\}$ the associated metric tensor, as defined in equation (2.2). Let $f : \Omega \to \mathbb{R}$ be a scalar function, $\vec{u} : \Omega \to \mathbb{R}^3$ a contravariant vector field given by $\vec{u} = u^1\mathbf{t}_1 + u^2\mathbf{t}_2 + u^3\mathbf{t}_3$, and $\mathbb{T} : \Omega \to \mathbb{R}^{3\times 3}$ a rank-2 contravariant tensor given by $\mathbb{T} = \left\{\tau^{ij}\right\}$. Then, the differential operators in the LCS are given by the following expressions.*

– *The gradient of f is:*

$$\nabla_{\mathcal{G}} f = \mathcal{G}^{-1} \nabla f = \left(\frac{1}{h_{(1)}^2} \frac{\partial f}{\partial s^1}, \frac{1}{h_{(2)}^2} \frac{\partial f}{\partial s^2}, \frac{\partial f}{\partial s^3} \right). \tag{2.4}$$

– *The divergence of $\vec{u}$ is:*

$$\nabla_{\mathcal{G}} \cdot \vec{u} = \frac{1}{\sqrt{\det(\mathcal{G})}} \nabla \cdot \left(\sqrt{\det(\mathcal{G})} \vec{u} \right) = \frac{1}{h_{(1)} h_{(2)}} \left(\frac{\partial \left(h_{(1)} h_{(2)} u^1 \right)}{\partial s^1} + \frac{\partial \left(h_{(1)} h_{(2)} u^2 \right)}{\partial s^2} + \frac{\partial \left(h_{(1)} h_{(2)} u^3 \right)}{\partial s^3} \right). \tag{2.5}$$

– *The jth component of the divergence $\mathbb{T}$ is:*

$$\begin{aligned} (\nabla_{\mathcal{G}} \cdot \mathbb{T})^j = \nabla_{\mathcal{G}_i} \tau^{ij} &= \frac{1}{\sqrt{\det(\mathcal{G})}} \frac{\partial}{\partial s^i} \left(\sqrt{\det(\mathcal{G})} \tau^{ij} \right) + \Gamma_{ik}^j \tau^{ik} \\ &= \nabla_{\mathcal{G}} \cdot \tau^{(\cdot j)} + \frac{1}{h_{(j)}} \left(2\tau^{1j} \frac{\partial h_{(j)}}{\partial s^1} - \tau^{11} \frac{h_{(1)}}{h_{(j)}} \frac{\partial h_{(1)}}{\partial s^j} \right) + \frac{1}{h_{(j)}} \left(2\tau^{2j} \frac{\partial h_{(j)}}{\partial s^2} - \tau^{22} \frac{h_{(2)}}{h_{(j)}} \frac{\partial h_{(2)}}{\partial s^j} \right), \end{aligned} \tag{2.6}$$

where $\nabla_{\mathcal{G}} \cdot \tau^{(\cdot j)}$ identifies the divergence of the jth column of $\mathbb{T}$, and Γ_{ij}^k denote the Christoffel symbols.

Remark 2.3. In the following, we will reduce our system to a two-dimensional tangent-following local system describing only points of the bottom surface by means of the coordinates s^1, s^2. In this case, the metric tensor reduces to the sub-tensor containing only the information related to those two directions. For simplicity, we will use the same symbols, equations, and operators in compact form independently of the spatial dimension, and the context will provide the appropriate definition.

2.2. Derivation of the SW model

The derivation of the SWE starts from the formulation of Navier–Stokes equations in the local coordinate system. Using Lemma 2.2, the Navier–Stokes equations given in equation (2.1) can be written in the LCS as:

$$\nabla_{\mathcal{G}} \cdot \vec{u} = 0, \tag{2.7a}$$

$$\frac{\partial \vec{u}}{\partial t} + \nabla_{\mathcal{G}} \cdot (\vec{u} \otimes \vec{u}) = -\frac{1}{\rho} \nabla_{\mathcal{G}} p + \frac{1}{\rho} \nabla_{\mathcal{G}} \cdot \mathbb{T} + \vec{g}. \tag{2.7b}$$

Next, we perform depth integration along s^3, the direction locally normal to the terrain surface running between the bottom and the free surfaces. We start this task by looking at the boundary conditions on these surfaces.

2.2.1. Boundary conditions

Using the LCS, the bottom and free surfaces are given by:

$$\begin{aligned} \mathcal{S}_{\mathcal{B}} &:= \left\{ (s^1, s^2, s^3) \in \mathbb{R}^3 \text{ such that } s^3 = \mathcal{B}(s^1, s^2) \equiv 0 \right\}, \\ \mathcal{S}_{\mathcal{F}} &:= \left\{ (s^1, s^2, s^3, t) \in \mathbb{R}^3 \times [0, T] \text{ such that } s^3 = \mathcal{F}(s^1, s^2, t) \equiv \eta(s^1, s^2, t) \right\}, \end{aligned}$$

where $\eta(s^1, s^2, t) = \mathcal{F}(s^1, s^2, t) - \mathcal{B}(s^1, s^2)$ denotes the fluid depth. We assume that the bottom is not eroding and thus maintains a fixed geometry, while the fluid surface is a function of time. The kinematic conditions postulate that the free surface moves with the fluid and that the bottom is impermeable. Thus we can write:

$$\frac{\mathrm{d}F_{\mathcal{M}}}{\mathrm{d}t} = \frac{\partial F_{\mathcal{M}}}{\partial t} + \vec{u} \cdot \nabla_{\mathcal{G}} F_{\mathcal{M}} \Big|_{\mathcal{M}} = 0,$$

where $\mathcal{M} = \mathcal{B}$ or $\mathcal{F}$. Since $F_{\mathcal{B}} = s^3 - \mathcal{B}(s^1, s^2)$ and $F_{\mathcal{F}} = s^3 - \mathcal{F}(s^1, s^2, t)$, we obtain immediately:

$$\frac{\mathrm{d}F_{\mathcal{B}}}{\mathrm{d}t} = \vec{u}\Big|_{\mathcal{B}} \cdot \nabla_{\mathcal{G}} F_{\mathcal{B}} = \vec{u} \cdot \nabla_{\mathcal{G}} F_{\mathcal{B}}\Big|_{s^3=0} = 0, \tag{2.8a}$$

$$\frac{\mathrm{d}F_{\mathcal{F}}}{\mathrm{d}t} = -\frac{\partial \eta}{\partial t} + \vec{u} \cdot \nabla_{\mathcal{G}} F_{\eta}\Big|_{s^3=\eta} = -\frac{\partial \eta}{\partial t} - \left(u^1 \frac{\partial \eta}{\partial s^1} + u^2 \frac{\partial \eta}{\partial s^2} - u^3 \right) \Big|_{s^3=\eta} = 0. \tag{2.8b}$$

Note that here we make use of the fact that the bottom surface is assumed to be independent of time, *i.e.*, $\partial\mathcal{B}/\partial t = 0$. Moreover, assuming that the external actions on the fluid surface are negligible, the dynamic condition at the fluid-air interface translates into a zero-stress boundary equation:

$$\mathbb{T}_{\mathcal{F}} \cdot \mathbf{N}_{\mathcal{F}} = 0, \quad \mathbf{N}_{\mathcal{F}} = \frac{\nabla \mathcal{F}}{||\nabla \mathcal{F}||} \tag{2.9}$$

where $\mathbf{N}_{\mathcal{F}}$ is the unit normal vector on the free surface $\mathcal{F}$. The bed boundary condition imposes the value of the shear stress:

$$\mathbb{T}_{\mathcal{B}} \cdot \mathbf{N}_{\mathcal{B}} = \tau_b^1 \mathbf{t}_1 + \tau_b^2 \mathbf{t}_2 + p_{\mathcal{B}} \mathbf{t}_3, \tag{2.10}$$

where $p_{\mathcal{B}}$ indicates the bottom pressure. The values for τ_b^i are expressed by means of classical steady-state empirical friction laws (*e.g.*, Chezy, Manning, or Gauckler–Strickler equations).

2.2.2. Depth integration of the Navier–Stokes equations

Starting from the Navier–Stokes equations written in the local curvilinear coordinate system as given in equation (2.7), we perform depth integration along the normal direction s^3 from $s^3 = \mathcal{B}(s^1, s^2) \equiv 0$ to $s^3 = \mathcal{F}(s^1, s^2, t) \equiv \eta(s^1, s^2, t)$. In the interest of space, we will omit the measure symbol $\mathrm{d}s^3$ in the integrals whenever no confusion arises.

The continuity equation (2.7a). Applying Leibniz rule and recalling the kinematic boundary conditions given by equation (2.8), we obtain:

$$\begin{aligned}
\int_0^\eta \nabla_{\mathcal{G}} \cdot \vec{u} &= \int_0^\eta \frac{1}{h_{(1)}h_{(2)}} \left(\frac{\partial \left(h_{(1)}h_{(2)}u^1\right)}{\partial s^1} + \frac{\partial \left(h_{(1)}h_{(2)}u^2\right)}{\partial s^2} + \frac{\partial \left(h_{(1)}h_{(2)}u^3\right)}{\partial s^3} \right) \\
&= \frac{1}{h_{(1)}h_{(2)}} \frac{\partial}{\partial s^1} \int_0^\eta h_{(1)}h_{(2)}u^1 + \frac{1}{h_{(1)}h_{(2)}} \frac{\partial}{\partial s^2} \int_0^\eta h_{(1)}h_{(2)}u^2 \\
&\quad + u^3\Big|_{s^3=\eta} - u^1 \frac{\partial \mathcal{F}}{\partial s^1}\Big|_{s^3=\eta} - u^2 \frac{\partial \mathcal{F}}{\partial s^2}\Big|_{s^3=\eta} \\
&\quad - u^3\Big|_{s^3=0} + u^1 \frac{\partial \mathcal{B}}{\partial s^1}\Big|_{s^3=0} + u^2 \frac{\partial \mathcal{B}}{\partial s^2}\Big|_{s^3=0} \\
&= \frac{\partial \eta}{\partial t} + \nabla_{\mathcal{G}} \cdot \int_0^\eta \underline{\vec{u}},
\end{aligned}$$

where $\underline{\vec{u}} := [u^1, u^2]^T$ and the curvilinear divergence operator $\nabla_{\mathcal{G}} \cdot$ is adapted to the two-dimensional setting (see Rem. 2.3). Recall that application of Leibniz rule requires enough regularity of both bottom and free surfaces as well as the velocity vector $\vec{u}$.

The momentum equation (2.7b). Integration along the s^3-direction yields:

$$\int_0^\eta \frac{\partial \vec{u}}{\partial t} + \int_0^\eta \nabla_{\mathcal{G}} \cdot (\vec{u} \otimes \vec{u}) = -\frac{1}{\rho} \int_0^\eta \nabla_{\mathcal{G}}\, p - g \int_0^\eta \nabla_{\mathcal{G}}\, x^3 + \frac{1}{\rho} \int_0^\eta \nabla_{\mathcal{G}} \cdot \mathbb{T}.$$

Employing Leibniz rule and the kinematic BC, the left-hand-side can be written as:

$$\begin{aligned}
&\frac{\partial}{\partial t} \int_0^\eta \vec{u} - \vec{u} \frac{\partial \eta}{\partial t} + \nabla_{\mathcal{G}} \cdot \int_0^\eta \vec{u} \otimes \vec{u} - (\vec{u} \otimes \vec{u}) \nabla_{\mathcal{G}}\, \mathcal{F}\Big|_{s^3=\eta} + (\vec{u} \otimes \vec{u}) \nabla_{\mathcal{G}}\, \mathcal{B}\Big|_{s^3=0} \\
&\quad = \frac{\partial}{\partial t} \int_0^\eta \vec{u} + \nabla_{\mathcal{G}} \cdot \int_0^\eta \vec{u} \otimes \vec{u} - \vec{u} \left(\frac{\partial \eta}{\partial t} + \vec{u} \cdot \nabla_{\mathcal{G}}\, \mathcal{F}\Big|_{s^3=\eta} \right) = \frac{\partial}{\partial t} \int_0^\eta \vec{u} + \nabla_{\mathcal{G}} \cdot \int_0^\eta \vec{u} \otimes \vec{u}.
\end{aligned}$$

Similar computations for the right-hand-side produce:

$$
\begin{aligned}
&-\frac{1}{\rho}\int_0^\eta \nabla_{\mathcal{G}}\, p - g\int_0^\eta \nabla_{\mathcal{G}}\, x^3 + \frac{1}{\rho}\nabla_{\mathcal{G}}\cdot\int_0^\eta \mathbb{T} - \frac{\mathbb{T}}{\rho}\nabla_{\mathcal{G}}\,\mathcal{F}\Big|_{s^3=\eta} + \frac{\mathbb{T}}{\rho}\nabla_{\mathcal{G}}\,\mathcal{B}\Big|_{s^3=0}\\
&\quad = -\frac{1}{\rho}\int_0^\eta \nabla_{\mathcal{G}}\, p - g\int_0^\eta \nabla_{\mathcal{G}}\, x^3 + \frac{1}{\rho}\nabla_{\mathcal{G}}\cdot\int_0^\eta \mathbb{T} + \frac{1}{\rho}\mathbb{T}_{\mathcal{B}}\cdot\mathbf{N}_{\mathcal{B}},
\end{aligned}
$$

where we made use here of the dynamic boundary conditions given in equations (2.9) and (2.10).

The normally integrated Navier–Stokes equations. Putting all the above calculations together we obtain the final system of normally integrated Navier–Stokes equations:

$$
\frac{\partial\eta}{\partial t} + \nabla_{\mathcal{G}}\cdot\int_0^\eta \underline{\vec{u}} = 0, \tag{2.11a}
$$

$$
\frac{\partial}{\partial t}\int_0^\eta \vec{u} + \nabla_{\mathcal{G}}\cdot\int_0^\eta \vec{u}\otimes\vec{u} = -\frac{1}{\rho}\int_0^\eta \nabla_{\mathcal{G}}\, p - g\int_0^\eta \nabla_{\mathcal{G}}\, x^3 + \frac{1}{\rho}\nabla_{\mathcal{G}}\cdot\int_0^\eta \mathbb{T} + \frac{1}{\rho}\mathbb{T}_{\mathcal{B}}\cdot\mathbf{N}_{\mathcal{B}}. \tag{2.11b}
$$

Here equation (2.11a) is a scalar equation while equation (2.11b) is a three-component system. In the following section, we derive the reduced two-component equations governing momentum balance by doing a formal order expansion and invoking the SW hypothesis.

2.2.3. Length scales and physical quantities

The classical SW hypothesis states that the characteristic depth of the fluid is smaller than the characteristic wavelength. In the present context, this statement is equivalent to our assumption of small normal velocity. To see this, assume a setting with a relatively thin and wide fluid moving on the terrain surface. Denote with L_0 the length scale in a direction tangential to the bottom and with H_0 the length scale of the fluid depth measured along the normal. The shallow water scaling assumes that $H_0/L_0 = \epsilon \ll 1$. We would like to connect this idea with the order of approximation of the model in our curvilinear setting.

Denote by V_0 the scale of the contravariant tangential velocity components u^1 and u^2, and by W_0 the scale of the contravariant normal component u^3. From the hypothesis of regularity of the bottom surface, the metric coefficients can be considered of order $\mathcal{O}(1)$, and represent just the length scale of the coordinate transformation between the GCS and the LCS. However, we do not have any *a priori* information on the order of magnitude of the derivatives of these metric coefficients. Formal application of the chain rule of differentiation to the continuity equation (2.7a) yields:

$$
\begin{aligned}
\nabla_{\mathcal{G}}\cdot\vec{u} &= \frac{1}{h_{(1)}h_{(2)}}\left(\frac{\partial}{\partial s^1}\left(h_{(1)}h_{(2)}u^1\right) + \frac{\partial}{\partial s^2}\left(h_{(1)}h_{(2)}u^2\right) + \frac{\partial}{\partial s^3}\left(h_{(1)}h_{(2)}u^3\right)\right)\\
&= \underbrace{\frac{\partial u^1}{\partial s^1}}_{\mathcal{O}\left(\frac{V_0}{L_0}\right)} + \underbrace{\frac{\partial u^2}{\partial s^2}}_{\mathcal{O}\left(\frac{V_0}{L_0}\right)} + \underbrace{\frac{\partial u^3}{\partial s^3}}_{\mathcal{O}\left(\frac{W_0}{H_0}\right)} + \underbrace{\frac{u^1}{h_{(1)}}}_{\mathcal{O}(V_0)}\frac{\partial h_{(1)}}{\partial s^1} + \underbrace{\frac{u^1}{h_{(2)}}}_{\mathcal{O}(V_0)}\frac{\partial h_{(2)}}{\partial s^1} + \underbrace{\frac{u^2}{h_{(1)}}}_{\mathcal{O}(V_0)}\frac{\partial h_{(1)}}{\partial s^2} + \underbrace{\frac{u^2}{h_{(2)}}}_{\mathcal{O}(V_0)}\frac{\partial h_{(2)}}{\partial s^2} = 0.
\end{aligned}
$$

Multiplying by H_0, we have that:

$$
\frac{H_0}{L_0}V_0 + W_0 + H_0V_0\max\left\{\frac{\partial h_{(1)}}{\partial s^1}, \frac{\partial h_{(2)}}{\partial s^1}, \frac{\partial h_{(1)}}{\partial s^2}, \frac{\partial h_{(2)}}{\partial s^2}\right\} \sim 0,
$$

from which we can estimate the scaling of the s^3-velocity as:

$$
W_0 \sim \max\left\{\epsilon, H_0\frac{\partial h_{(1)}}{\partial s^1}, H_0\frac{\partial h_{(2)}}{\partial s^1}, H_0\frac{\partial h_{(1)}}{\partial s^2}, H_0\frac{\partial h_{(2)}}{\partial s^2}\right\}V_0 = \epsilon_{\mathcal{G}}V_0. \tag{2.12}
$$

This defines a "geometric" aspect ratio $\epsilon_{\mathcal{G}}$ given by:

$$\epsilon_{\mathcal{G}} := \max\left\{\epsilon, H_0\frac{\partial h_{(1)}}{\partial s^1}, H_0\frac{\partial h_{(2)}}{\partial s^1}, H_0\frac{\partial h_{(1)}}{\partial s^2}, H_0\frac{\partial h_{(2)}}{\partial s^2}\right\}, \tag{2.13}$$

that connects local curvatures information to the global length scale parameter ϵ. Hence, the SW approximation can be restated by the assumption $\epsilon_{\mathcal{G}} \ll 1$, which effectively adds a restriction on the shape of the bottom surface that ensures that the derivatives of the metric coefficients are of the order of $1/L_0$. Note that this assumption is satisfied if the principal curvatures of the bottom surface are bounded by const/L_0. This limitation is inherent to our model setup and is shared also by the models in [10,18].

2.2.4. Formal order of approximation and the SW hypothesis

Starting from the integrated Navier–Stokes equations in the curvilinear coordinate system shown in equation (2.11), we proceed by applying the SW hypothesis. Thus we postulate that the fluid motion is much faster in the tangential directions than in the normal direction, *i.e.*, $u^3 = \epsilon_{\mathcal{G}} u^i$, $i = 1, 2$, $\epsilon_{\mathcal{G}} \ll 1$, and we expand the components of the velocity vector in powers of the parameter $\epsilon_{\mathcal{G}}$:

$$u^i = u^i_{(0)} + \epsilon_{\mathcal{G}} u^i_{(1)} + \epsilon^2_{\mathcal{G}} u^i_{(2)} + \mathcal{O}\big(\epsilon^3_{\mathcal{G}}\big) \quad i = 1, 2, \tag{2.14a}$$

$$u^3 = \epsilon_{\mathcal{G}} u^3_{(1)} + \epsilon^2_{\mathcal{G}} u^3_{(2)} + \mathcal{O}\big(\epsilon^3_{\mathcal{G}}\big)\,. \tag{2.14b}$$

We also expand the general stress tensor components using the same parameter $\epsilon_{\mathcal{G}}$ to obtain:

$$\tau^{ij} = \tau^{ij}_{(0)} + \epsilon_{\mathcal{G}} \tau^{ij}_{(1)} + \epsilon^2_{\mathcal{G}} \tau^{ij}_{(2)} + \mathcal{O}\big(\epsilon^3_{\mathcal{G}}\big) \quad i, j = 1, 2, 3. \tag{2.15}$$

Again, we assume that the terms $\tau^{i3} = \tau^{3i}$, $i = 1, 2, 3$, which contain u^3, can be expanded as:

$$\tau^{3i} = \epsilon_{\mathcal{G}} \tau^{3i}_{(1)} + \epsilon^2_{\mathcal{G}} \tau^{3i}_{(2)} + \mathcal{O}\big(\epsilon^3_{\mathcal{G}}\big) \quad \text{for} \quad i = 1, 2, \quad \text{and} \quad \tau^{33} = \epsilon^2_{\mathcal{G}} \tau^{33}_{(2)} + \mathcal{O}\big(\epsilon^3_{\mathcal{G}}\big)\,.$$

We split the velocity vector and stress tensor as the sum of the corresponding average values $\vec{U}$ and $\mathbf{T}$ and fluctuations $\tilde{u}$ and $\tilde{\tau}$ around the mean. Thus we write:

$$\vec{u} = \vec{U} + \tilde{u}, \quad \text{where} \quad \vec{U}\,(s^1, s^2, t) = \frac{1}{\eta}\int_0^\eta \vec{u}\,(\mathbf{s}, t)\ \mathrm{d}s^3, \quad \int_0^\eta \tilde{u}\,(\mathbf{s}, t)\ \mathrm{d}s^3 = 0, \tag{2.16}$$

$$\mathbb{T} = \mathbf{T} + \tilde{\tau}, \quad \text{where} \quad \mathbf{T}\,(s^1, s^2, t) = \frac{1}{\eta}\int_0^\eta \mathbb{T}\,(\mathbf{s}, t)\ \mathrm{d}s^3, \quad \int_0^\eta \tilde{\tau}\,(\mathbf{s}, t)\ \mathrm{d}s^3 = 0. \tag{2.17}$$

Expansions in powers of $\epsilon_{\mathcal{G}}$ are readily written for all these quantities. Using equations (2.16) and (2.17), depth integration of $\vec{u}$ and $\mathbb{T}$ yields:

$$\int_0^\eta \vec{u} = \int_0^\eta \left(\vec{U} + \tilde{u}\right) = \eta\vec{U}, \quad \int_0^\eta \mathbb{T} = \int_0^\eta (\mathbf{T} + \tilde{\tau}) = \eta\mathbf{T}.$$

The depth-averaged tensor continues to display velocity fluctuations and can be expressed as:

$$\int_0^\eta \vec{u} \otimes \vec{u} = \int_0^\eta \left(\vec{U} + \tilde{u}\right) \otimes \left(\vec{U} + \tilde{u}\right) = \eta\vec{U} \otimes \vec{U} + \int_0^\eta \tilde{u} \otimes \tilde{u},$$

where the fluctuation tensor $\tilde{u} \otimes \tilde{u}$ associated with $\vec{u}$ has the same form of $\mathbb{T}$, and is considered incorporated in it.

The intrinsic shallow water equations. Using the formal expansions in powers of $\epsilon_{\mathcal{G}}$ in the normally integrated NS system equation (2.11) we obtain our reduced formulation, which we name Intrinsic Shallow Water Equations (ISWE), as given in the next theorem. We use the following notation. The couple (s^1, s^2) indicates the curvilinear coordinate system associated with the LCS defined in equation (2.3) with the ensuing metric tensor $\mathcal{G}_{sw}$ given by the principal 2-minor of equation (2.2). The vector $\vec{q} = \left[\eta U^1, \eta U^2\right]^T$ denotes the depth-averaged velocity vector, while the tensor

$$\mathbf{T}_{sw} = \eta \begin{bmatrix} \mathbf{T}^{11} & \mathbf{T}^{12} \\ \mathbf{T}^{21} & \mathbf{T}^{22} \end{bmatrix}$$

is the principal 2-minors of $\mathbf{T}$. Vector $\mathbf{f}_{\mathcal{B}} = \left[\tau_b^1, \tau_b^2\right]^T$ is the vector field accounting for bed friction. The we can state the following theorem.

Theorem 2.4. *The intrinsic shallow water equations, written with respect to the LCS (Eqs. (2.2) and (2.3)), are given by:*

$$\frac{\partial \eta}{\partial t} + \nabla_{\mathcal{G}} \cdot \vec{q} = 0, \tag{2.18a}$$

$$\frac{\partial \vec{q}}{\partial t} + \nabla_{\mathcal{G}} \cdot \left(\frac{1}{\eta} (\vec{q} \otimes \vec{q}) + \left(\frac{g\eta^2}{2} \frac{\partial x^3}{\partial s^3} \right) \mathcal{G}_{sw}^{-1} \right) + \frac{g\eta^2}{2} \nabla_{\mathcal{G}} \left(\frac{\partial x^3}{\partial s^3} \right) + g\eta \nabla_{\mathcal{G}} (x^3) - \frac{1}{\rho} (\nabla_{\mathcal{G}} \cdot \mathbf{T}_{sw} + \mathbf{f}_{\mathcal{B}}) = 0. \tag{2.18b}$$

They provide an approximation of order $\mathcal{O}(\epsilon_{\mathcal{G}}^2)$ of the Navier–Stokes equations, under the assumption of thin fluid layer, $\eta = \mathcal{O}(\epsilon_{\mathcal{G}})$.

Proof. We start by re-writing equation (2.11b) component-wise. Using the operators defined in Lemma 2.2 and recalling that the terms $\partial h_{(1)}/\partial s^3, \partial h_{(2)}/\partial s^3$ vanish, the third equation, describing momentum conservation along s^3, takes on the form:

$$\begin{aligned} &\frac{\partial}{\partial t} \int_0^\eta u^3 + \frac{1}{h_{(1)} h_{(2)}} \left(\frac{\partial}{\partial s^1} \int_0^\eta h_{(1)} h_{(2)} u^1 u^3 + \frac{\partial}{\partial s^2} \int_0^\eta h_{(1)} h_{(2)} u^2 u^3 + \frac{\partial}{\partial s^3} \int_0^\eta h_{(1)} h_{(2)} \left(u^3\right)^2 \right) \\ &\quad = -\frac{1}{\rho} \int_0^\eta \frac{\partial p}{\partial s^3} - g \int_0^\eta \frac{\partial x^3}{\partial s^3} + \frac{1}{\rho h_{(1)} h_{(2)}} \left(\frac{\partial}{\partial s^1} \int_0^\eta h_{(1)} h_{(2)} \tau^{31} + \frac{\partial}{\partial s^2} \int_0^\eta h_{(1)} h_{(2)} \tau^{32} \right. \\ &\qquad \left. + \frac{\partial}{\partial s^3} \int_0^\eta h_{(1)} h_{(2)} \tau^{33} \right) + \frac{p_{\mathcal{B}}}{\rho}, \end{aligned}$$

where $p_{\mathcal{B}}$ is the bed pressure as given in equation (2.10). Introducing the expanded velocity, equation (2.14), and tensor components, equation (2.15), we obtain

$$\begin{aligned} &\frac{1}{\rho} \int_0^\eta \frac{\partial p}{\partial s^3} + g \int_0^\eta \frac{\partial x^3}{\partial s^3} \\ &\quad + \epsilon_{\mathcal{G}} \left[\frac{\partial}{\partial t} \left(\eta U_{(1)}^3 \right) + \frac{1}{h_{(1)} h_{(2)}} \left(\frac{\partial}{\partial s^1} \left(\eta U_{(0)}^1 U_{(1)}^3 h_{(1)} h_{(2)} \right) + \frac{\partial}{\partial s^2} \left(\eta U_{(0)}^2 U_{(1)}^3 h_{(1)} h_{(2)} \right) \right) \right. \\ &\quad \left. - \frac{1}{\rho h_{(1)} h_{(2)}} \left(\frac{\partial}{\partial s^1} \int_0^\eta \tau_{(1)}^{31} h_{(1)} h_{(2)} + \frac{\partial}{\partial s^2} \int_0^\eta \tau_{(1)}^{32} h_{(1)} h_{(2)} \right) + \frac{p_{\mathcal{B},(1)}}{\rho} \right] + \mathcal{O}(\epsilon_{\mathcal{G}}^2) = 0, \end{aligned} \tag{2.19}$$

where the term $p_{\mathcal{B},(1)}$, the s^3-component of the shear stress $\mathbb{T}_{\mathcal{B}} \cdot \mathbf{N}_{\mathcal{B}}$, is a first order approximation (as evidenced by the (1) subscript) and thus is assumed to be proportional to $\epsilon_{\mathcal{G}}$. Looking at the zero-order terms, *i.e.*, the terms proportional to $\epsilon_{\mathcal{G}}^0$, we can write:

$$\frac{1}{\rho} \int_0^\eta \frac{\partial p}{\partial s^3} + g \int_0^\eta \frac{\partial x^3}{\partial s^3} = \mathcal{O}(\epsilon_{\mathcal{G}})$$

that corresponds to the hydrostatic pressure condition along the normal direction to the bottom surface. Since we neglect the effects of surface tension and wind on the free surface, we can set $p\Big|_{s^3=\eta} = p_{\text{atm}} = 0$, to obtain:

$$p\Big|_0 = \rho g \eta \frac{\partial x^3}{\partial s^3} + \mathcal{O}(\epsilon_{\mathcal{G}})\,. \tag{2.20}$$

Recall that the term $\frac{\partial x^3}{\partial s^3}$ does not depend on s^3, since we are assuming the direction s^3 to be rectilinear.

This condition states, up to terms of order $\epsilon_{\mathcal{G}}$, that the fluid pressure varies linearly along the s^3 direction. Substitution of this algebraic expression for the pressure ensures the actual reduction of the system of PDEs from four to three equations, as in the classical SWE derivation.

We turn now our attention to the other two components of equation (2.11b). Focusing only on the s^1-equation, the other being analogous, we can write:

$$\begin{aligned}
&\frac{\partial}{\partial t}\int_0^\eta u^1 + \frac{1}{h_{(1)}h_{(2)}}\left[\frac{\partial}{\partial s^1}\int_0^\eta h_{(1)}h_{(2)}\left(u^1\right)^2 + \frac{\partial}{\partial s^2}\int_0^\eta h_{(1)}h_{(2)}u^1u^2 + \frac{\partial}{\partial s^3}\int_0^\eta h_{(1)}h_{(2)}u^3u^1\right] \\
&\qquad + \int_0^\eta \frac{\left(u^1\right)^2}{h_{(1)}}\frac{\partial h_{(1)}}{\partial s^1} + 2\int_0^\eta \frac{u^1u^2}{h_{(1)}}\frac{\partial h_{(1)}}{\partial s^2} - \int_0^\eta \left(u^2\right)^2\frac{h_{(2)}}{h_{(1)}^2}\frac{\partial h_{(2)}}{\partial s^1} \\
&= -\frac{1}{\rho}\int_0^\eta \frac{1}{h_{(1)}^2}\frac{\partial p}{\partial s^1} - g\int_0^\eta \frac{1}{h_{(1)}^2}\frac{\partial x^3}{\partial s^1} + \frac{1}{\rho h_{(1)}h_{(2)}}\left[\frac{\partial}{\partial s^1}\int_0^\eta h_{(1)}h_{(2)}\tau^{11} + \frac{\partial}{\partial s^2}\int_0^\eta h_{(1)}h_{(2)}\tau^{12}\right. \\
&\qquad \left. + \frac{\partial}{\partial s^3}\int_0^\eta h_{(1)}h_{(2)}\tau^{13}\right] + \frac{1}{\rho}\left(\int_0^\eta \frac{\tau^{11}}{h_{(1)}}\frac{\partial h_{(1)}}{\partial s^1} + 2\int_0^\eta \frac{\tau^{21}}{h_{(1)}}\frac{\partial h_{(1)}}{\partial s^2} - \int_0^\eta \tau^{22}\frac{h_{(2)}}{h_{(1)}^2}\frac{\partial h_{(2)}}{\partial s^1}\right) + \frac{\tau_b^1}{\rho}.
\end{aligned}$$

Again, we enforce an approximation of order $\epsilon_{\mathcal{G}}$ and recalling the expansions in equations (2.14) and (2.15), we obtain:

– for the left-hand-side

$$\begin{aligned}
&\frac{\partial \eta U^1_{(0)}}{\partial t} + \frac{1}{h_{(1)}h_{(2)}}\frac{\partial}{\partial s^1}\left(\eta\left(U^1_{(0)}\right)^2 h_{(1)}h_{(2)}\right) + \frac{1}{h_{(1)}h_{(2)}}\frac{\partial}{\partial s^2}\left(\eta U^1_{(0)}U^2_{(0)}h_{(1)}h_{(2)}\right) \\
&\qquad + \eta\left(U^1_{(0)}\right)^2\frac{1}{h_{(1)}}\frac{\partial h_{(1)}}{\partial s^1} + 2\eta U^1_{(0)}U^2_{(0)}\frac{1}{h_{(1)}}\frac{\partial h_{(1)}}{\partial s^2} - \eta\left(U^2_{(0)}\right)^2\frac{h_{(2)}}{h_{(1)}^2}\frac{\partial h_{(2)}}{\partial s^1} + \mathcal{O}(\epsilon_{\mathcal{G}})\,;
\end{aligned}$$

– for the right-hand-side

$$\begin{aligned}
&-\frac{\eta}{\rho h_{(1)}^2}\frac{\partial p}{\partial s^1} - \frac{\eta g}{h_{(1)}^2}\frac{\partial x^3}{\partial s^1} + \frac{1}{\rho h_{(1)}h_{(2)}}\left[\frac{\partial}{\partial s^1}\int_0^\eta \tau^{11}_{(0)}h_{(1)}h_{(2)} + \frac{\partial}{\partial s^2}\int_0^\eta \tau^{12}_{(0)}h_{(1)}h_{(2)}\right] \\
&\qquad + \frac{1}{\rho h_{(1)}}\frac{\partial h_{(1)}}{\partial s^1}\int_0^\eta \tau^{11}_{(0)} + \frac{2}{\rho h_{(1)}}\frac{\partial h_{(1)}}{\partial s^2}\int_0^\eta \tau^{12}_{(0)} - \frac{h_{(2)}}{\rho h_{(1)}^2}\frac{\partial h_{(2)}}{\partial s^1}\int_0^\eta \tau^{22}_{(0)} + \frac{\tau_b^1{}_{(0)}}{\rho} + \mathcal{O}(\epsilon_{\mathcal{G}})\,.
\end{aligned}$$

Inserting the expression for the pressure given in equation (2.20) yields:

$$-\frac{\eta}{h_{(1)}^2}\frac{\partial}{\partial s^1}\left(\eta g\frac{\partial x^3}{\partial s^3}\right) - \frac{\eta g}{h_{(1)}^2}\frac{\partial x^3}{\partial s^1} + \frac{1}{\rho}\left(\nabla_{\mathcal{G}}\cdot\mathbf{T}_{sw,(0)}\right)^1 + \frac{\tau_b^1{}_{(0)}}{\rho} + \mathcal{O}(\epsilon_{\mathcal{G}})\,.$$

The final divergence form of the model is obtained by applying the chain rule on the first term of the previous equation. This implies the assumption that the depth function η and $\frac{\partial x^3}{\partial s^3}$ are differentiable functions. We obtain:

$$\frac{\eta}{h_{(1)}^2}\frac{\partial}{\partial s^1}\left(\eta g\frac{\partial x^3}{\partial s^3}\right) = \frac{g}{h_{(1)}^2}\frac{\partial}{\partial s^1}\left(\frac{\eta^2}{2}\frac{\partial x^3}{\partial s^3}\right) + \frac{g\eta^2}{2h_{(1)}^2}\frac{\partial}{\partial s^1}\left(\frac{\partial x^3}{\partial s^3}\right).$$

Recalling the definition of $\vec{q}$, the momentum equation can be re-written in compact form intrinsic to the bottom surface as:

$$\frac{\partial \vec{q}}{\partial t} + \nabla_{\mathcal{G}} \cdot \left(\frac{1}{\eta} \left(\vec{q} \otimes \vec{q} \right) + \left(\frac{g\eta^2}{2} \frac{\partial x^3}{\partial s^3} \right) \mathcal{G}_{sw}^{-1} \right) + \frac{g\eta^2}{2} \nabla_{\mathcal{G}} \left(\frac{\partial x^3}{\partial s^3} \right) + g\eta \nabla_{\mathcal{G}} \left(x^3 \right) - \frac{1}{\rho} \nabla_{\mathcal{G}} \cdot \mathbf{T}_{sw} - \frac{\mathbf{f}_{\mathcal{B}}}{\rho} + \mathcal{O}(\eta \, \epsilon_{\mathcal{G}}) = 0.$$

Note that in the last equation we have explicitly included in the higher order terms the proportionality to η, which is implicitly considered also in the previous equations. Hence, if we add the further assumption of $\eta = \mathcal{O}(\epsilon_{\mathcal{G}})$ the final form of the momentum equation is an approximation of order $\mathcal{O}\left(\epsilon_{\mathcal{G}}^2\right)$. Finally, note that the continuity equation (2.11a) is exact because of the intrinsic nature of the starting equation, and does not alter the order of approximation. □

2.3. Properties of the model

As already mentioned in the introduction, the ISWE model is similar to the model proposed by [10]. The most important improvement of our new formulation equation (2.18) is that only geometric terms appear in the source term and that the full divergence form is maintained for the conserved quantities. In addition to securing a more compact form of the equations, our formulation allows the development of a fully intrinsic discretization as will be seen in Section 3. Here we prove some fundamental mathematical properties, namely that the proposed model is invariant under rotation, it admits an energy equation, and is well-balanced (preserves the steady state of lake-at-rest).

Proposition 2.5. *The ISWE system defined in equation (2.18) is invariant under rotation, it admits a conserved energy in the absence of stresses, and is well-balanced.*

Proof. The first statement is proved by showing that all involved operators are rotation invariant. Consider first the gradient operator $\nabla_{\mathcal{G}}$. For any function $f : \Omega \to \mathbb{R}$, where $\Omega \subset \mathbb{R}^2$, and for any rotation operator $R \in \mathbb{R}^{2\times 2}$, the following relation holds:

$$\nabla_{\mathcal{G}} \tilde{f}(x) = R^T \nabla_{\mathcal{G}}^R f\left(\tilde{x}\right) \Big|_{\tilde{x}=Rx},$$

where $\tilde{f}(x) = f(Rx)$, and $\nabla_{\mathcal{G}}^R$ is the gradient operator in the rotated coordinates. This follows immediately from the application of the chain rule formula. Concerning the divergence operator, we consider first its application to a vector-valued function $u : \Omega \to \mathbb{R}^2$. We have:

$$\nabla_{\mathcal{G}} \cdot \tilde{u} = \nabla_{\mathcal{G}}^R \cdot u \Big|_{\tilde{x}=Rx},$$

where $\tilde{u} = R^T u$ is the rotated vector, and $\nabla_{\mathcal{G}}^R \cdot$ is the divergence in the rotated coordinate system. With the same notation, the following holds for the divergence of a tensor product $u \otimes u$:

$$\begin{aligned} \nabla_{\mathcal{G}}^R \cdot (\tilde{u} \otimes \tilde{u}) &= \tilde{u} \cdot \nabla_{\mathcal{G}}^R \tilde{u} + \tilde{u} \nabla_{\mathcal{G}}^R \cdot \tilde{u} = \left(R^T u \cdot R^T \nabla_{\mathcal{G}} \right) R^T u + R^T u \nabla_{\mathcal{G}} \cdot u \\ &= R^T \left(u \cdot \nabla_{\mathcal{G}} u + u \nabla_{\mathcal{G}} \cdot u \right) = R^T \nabla_{\mathcal{G}} \cdot (u \otimes u). \end{aligned}$$

The rotational invariance of equation (2.18) follows by noting that the above relation can be directly extended also to a diagonal tensor.

The energy expression for the system in equation (2.18) can be derived by setting $\mathbf{T}_{sw} = 0$ and $\mathbf{f}_{\mathcal{B}} = 0$ (zero stress) in equation (2.18b). Scalar multiplication by the conservative velocity $\vec{U}$ and application of the chain rule yields the energy equation for the system:

$$\frac{\partial}{\partial t} \left(\eta \frac{\left| \vec{U} \right|_{\mathcal{G}}^2}{2} + \frac{1}{2} g \eta^2 \frac{\partial x^3}{\partial s^3} + g x_{\mathcal{B}}^3 \eta \right) + \nabla_{\mathcal{G}} \cdot \left[\left(\eta \frac{\left| \vec{U} \right|_{\mathcal{G}}^2}{2} + \frac{1}{2} g \eta^2 \frac{\partial x^3}{\partial s^3} + g x_{\mathcal{B}}^3 \eta + \frac{1}{2} g \eta^2 \frac{\partial x^3}{\partial s^3} \right) \vec{U} \right] = 0,$$

where $x^3_{\mathcal{B}}$ is the elevation of the bottom with respect to the the GCS, and

$$\mathcal{E} = \eta \frac{\left|\vec{U}\right|^2_{\mathcal{G}}}{2} + \frac{1}{2} g \eta^2 \frac{\partial x^3}{\partial s^3} + g x^3_{\mathcal{B}} \eta, \quad p = \frac{1}{2} g \eta^2 \frac{\partial x^3}{\partial s^3}$$

are the kinetic energy and the pressure term, respectively.

Next, we show that the system is well-balanced, in the sense that it preserves the steady-state of a lake-at-rest. Let the functions $\eta = \eta(s^1, s^2)$ and $\vec{q} = \vec{q}(s^1, s^2)$ be time independent. Then, the model results in a zero velocity field and thus the steady-state for a horizontal free fluid surface (lake-at-rest) is preserved. Explicitly, from the mass conservation equation we get $\vec{U} = 0$, and from the momentum equation we obtain the following relation for the depth of the fluid:

$$\eta \frac{\partial x^3}{\partial s^3} + x^3_{\mathcal{B}} = \text{const.} \tag{2.21}$$

□

Remark 2.6. It is possible to generalize this result in the presence of stresses, obtaining a relation of the following form:

$$\frac{\partial}{\partial t}\left(\eta \frac{\left|\vec{U}\right|^2}{2} + \frac{1}{2} g \eta^2 \frac{\partial x^3}{\partial s^3} + g x^3 \eta\right) + \nabla_{\mathcal{G}} \cdot \left[\left(\eta \frac{\left|\vec{U}\right|^2}{2} + \frac{1}{2} g \eta^2 \frac{\partial x^3}{\partial s^3} + g x^3 \eta + \frac{1}{2} g \eta^2 \frac{\partial x^3}{\partial s^3}\right) \vec{U}\right]$$
$$= \frac{1}{\rho}\left[\nabla_{\mathcal{G}} \cdot \left(\mathbf{T}_{sw} \vec{U}\right) - \nabla_{\mathcal{G}} \vec{U} : \mathbf{T}_{sw} + \vec{U} \cdot \mathbf{f}_{\mathcal{B}}\right].$$

From this equation, using an energetically consistent model of the stress terms, an expression for the dissipation of the total energy can be obtained [12].

2.3.1. Comparison with other literature models

We conclude this section by listing the most important similarities and differences of our approach with respect to the models developed in [10, 18], which form our starting point. All three models share similar approximations characteristics, namely $\mathcal{O}(\epsilon^2)$ for small depths, contain the effects of bottom surface curvatures directly in the equations, and assume a linear velocity distribution along the normal. Moreover, they employ a local coordinate system anchored on the bottom surface.

The most important difference introduced in our methodology is that we make use exclusively of geometrically intrinsic quantities. This allows us to obtain a balance law formulation with a source term that, unlike the other two approaches, does not contain the velocity vector. For this reason, we are able to derive in the following sections a fully intrinsic numerical discretization exploiting the divergence theorem directly defined on the surface, thus maintaining all the original symmetries of the continuous model. In addition, discrete well-balance is readily enforced using standard techniques, such as the one suggested by [5].

3. Intrinsic finite volume scheme

We assume that our final system (2.18) is defined on a compact subset of the bottom surface, $\Gamma \subset \mathcal{S}_{\mathcal{B}}$, and that a well-defined curvilinear boundary, denoted by $\partial\Gamma = \partial\overline{\Gamma}$, exists. System (2.18) can be written in divergence form as the balance law:

$$\frac{\partial \mathbf{U}}{\partial t} + \operatorname{div}_{\mathcal{G}} \underline{\underline{F}}(\mathbf{s}, \mathbf{U}) + \mathbf{S}(\mathbf{s}, \mathbf{U}) = 0. \tag{3.1}$$

Here the conservative variable is given by $\mathbf{U} = \left[\eta, \eta U^1, \eta U^2\right]^T = \left[\eta, q^1, q^2\right]^T$, where $\eta : \Gamma \times [0,T] \to \mathbb{R}$, and $\mathbf{q} = \left[q^1, q^2\right]$, $\mathbf{q} : \Gamma \times [0,T] \to \mathbb{R}^2$. The flux function $\underline{\underline{F}}$ takes the form

$$\underline{\underline{F}}(\mathbf{s}, \mathbf{U}) = \begin{bmatrix} q^1 & q^2 \\ \dfrac{\left(q^1\right)^2}{\eta} + \dfrac{g\eta^2}{2h_{(1)}^2}\dfrac{\partial x^3}{\partial s^3} & \dfrac{q^1 q^2}{\eta} \\ \dfrac{q^1 q^2}{\eta} & \dfrac{\left(q^2\right)^2}{\eta} + \dfrac{g\eta^2}{2h_{(2)}^2}\dfrac{\partial x^3}{\partial s^3} \end{bmatrix} = \begin{bmatrix} \underline{F}^{\eta} \\ \underline{\underline{F}}^{\mathbf{q}} \end{bmatrix}. \tag{3.2}$$

Note that the flux $\underline{\underline{F}}$ is a function of $\mathbf{s}$ because of the appearance of the components $h_{(i)}$ of the metric tensor $\mathcal{G}_{sw}$ and the presence of the bottom slope $\partial x^3/\partial s^3$. The symbol $\mathrm{div}_{\mathcal{G}}$ denotes the divergence operator applied to the flux function as divergence of a vector for the first row and divergence of a 2×2 tensor for the last two rows. We can define it as $\mathrm{div}_{\mathcal{G}} = [\nabla_{\mathcal{G}}^{\eta} \cdot, \nabla_{\mathcal{G}}^{\mathbf{q}} \cdot]^T$. The source function $\mathbf{S}$ comprises the metric tensor coefficients, the bottom slope and its derivatives, the two-dimensional averaged stress tensor $\mathbf{T}_{sw}$, the bottom friction parameter τ_b, and the conserved variable η. We summarize this dependency by explicitly writing it out in $\mathbf{S}(\mathbf{s}, \eta)$. We have then:

$$\mathbf{S}(\mathbf{s}, \eta) = \begin{bmatrix} 0 \\ \dfrac{g\eta^2}{2h_{(1)}^2}\dfrac{\partial}{\partial s^1}\left(\dfrac{\partial x^3}{\partial s^3}\right) + \dfrac{g\eta}{h_{(1)}^2}\dfrac{\partial x^3}{\partial s^1} - \dfrac{1}{\rho}\left[\nabla_{\mathcal{G}} \cdot \mathbf{T}_{sw}\right]^{(1,\cdot)} - \dfrac{\tau_b^1}{\rho} \\ \dfrac{g\eta^2}{2h_{(2)}^2}\dfrac{\partial}{\partial s^2}\left(\dfrac{\partial x^3}{\partial s^3}\right) + \dfrac{g\eta}{h_{(2)}^2}\dfrac{\partial x^3}{\partial s^2} - \dfrac{1}{\rho}\left[\nabla_{\mathcal{G}} \cdot \mathbf{T}_{sw}\right]^{(2,\cdot)} - \dfrac{\tau_b^2}{\rho} \end{bmatrix} = \begin{bmatrix} S^{\eta} \\ \mathbf{S}^{\mathbf{q}} \end{bmatrix}. \tag{3.3}$$

The regularity assumption on the bottom surface implies the uniform continuity of the flux and source functions with respect to $\mathbf{s}$.

Our aim is to develop a first order upwind Godunov-type Finite Volume scheme defined intrinsically on the LCS coordinate system. The aim is to derive intrinsic definitions of the geometric differential operators. The derivation of the scheme starts from the definition of the computational mesh. We assume that there exists a surface triangulation $\mathcal{T}(\Gamma)$ formed by the union of non-intersecting geodesic triangles with vertices on Γ (edges are geodesics). Obviously, we have that $\mathcal{T}(\Gamma) = \cup_{i=1}^{N_T} T_i = \overline{\Gamma}$ and $\sigma_{ij} = T_i \cap T_j$ is an internal geodesic edge. We will also use the approximate triangulation $\mathcal{T}_h(\Gamma)$ defined by the piecewise linear surface identified by the union of 2-simplices in $\mathbb{R}^3$ (flat three-dimensional triangles) with vertices coinciding with the vertices of $\mathcal{T}(\Gamma)$. We assume that this triangulation is closely inscribed in $\mathcal{T}(\Gamma)$ in the sense of [28] (the tangent spaces of $\mathcal{T}(\Gamma)$ and of $\mathcal{T}_h(\Gamma)$ are close in some sense). Given a point $m \in T_h$, we indicate with $\mathrm{pr}(m)$ the point in $T \subset \mathcal{T}(\Gamma)$ of which m is the orthogonal projection along the surface normal direction $\mathbf{N}(\mathrm{pr}(m))$. We say that $\mathcal{T}_h(\Gamma)$ is closely inscribed in $\mathcal{T}(\Gamma)$ if every $T_h \in \mathcal{T}_h(\Gamma)$ lies within a neighborhood $\mathcal{N}_{\mathrm{pr}(m)}$ of $\mathcal{T}(\Gamma)$ such that $\mathrm{pr}(m)$ is well-defined and one-to-one for all $m \in T_h$. Quantities belonging to the approximated triangulation $\mathcal{T}_h(\Gamma)$ will be identified with the subscript h. Thus the symbol $\sigma_{h,ij}$ will identify the common edge between triangles $T_{h,i}$ and $T_{h,j}$. We will denote by $\mathcal{A}_T$ ($\mathcal{A}_i$) the area of cell T (T_i) in $\mathcal{T}(\Gamma)$, and by $\mathcal{A}_{T_h}$ ($\mathcal{A}_{h,i}$) the corresponding area in $\mathcal{T}_h(\Gamma)$. Analogously, we will denote with ℓ_σ (ℓ_{ij}) the length of the geodesic edge σ (σ_{ij}) in $\mathcal{T}(\Gamma)$, and ℓ_{σ_h} ($\ell_{h,ij}$) the corresponding length in $\mathcal{T}_h(\Gamma)$.

We start our work on $\mathcal{T}(\Gamma)$, where the divergence and integration by parts theorems are naturally defined. Following a standard development workflow for FV methods, we test equation (3.1) with a piecewise constant (in space and time) function and apply the divergence theorem to obtain the following set of equations valid for all triangles $T_i \in \mathcal{T}(\Gamma)$ and for $t \in \left[t^k, t^{k+1}\right]$:

$$\mathbf{U}_i^{k+1} = \mathbf{U}_i^k - \frac{1}{\mathcal{A}_i}\sum_{j=1}^{N_{\sigma(i)}} \ell_{ij} \int_{t^k}^{t^{k+1}} \mathbf{F}_{ij}(\mathbf{U})\, \mathrm{d}t - \int_{t^k}^{t^{k+1}} \mathbf{S}_i(\eta)\, \mathrm{d}t,$$

where we use the cell-averaged and edge-averaged quantities defined intrinsically in $\mathcal{T}(\Gamma)$ as:

$$\mathbf{U}_i = \frac{1}{\mathcal{A}_i}\int_{T_i}\mathbf{U}\,\mathrm{d}\mathbf{s}, \quad \mathbf{F}_{ij} = \frac{1}{\ell_{ij}}\int_{\sigma_{ij}}\left\langle \underline{\underline{F}}, \nu_{ij}\right\rangle_{\mathcal{G}}\mathrm{d}\sigma, \quad \mathbf{S}_i = \frac{1}{\mathcal{A}_i}\int_{T_i}\mathbf{S}\,\mathrm{d}\mathbf{s}, \tag{3.4}$$

and ν_{ij} is the local vector of the tangent plane normal to the edge σ_{ij} and pointing outward of the cell T_i. Note that the quantities $\mathbf{F}_{ij}, \mathbf{S}_i$ are depending only on the unknown $\mathbf{U}$ but not on the space variable $\mathbf{s}$, since they are integrated in space. Moreover, it is important to underline that no numerical approximations are done up to this point. Now we need to devise numerically computable approximations of the above quantities. Thus, the following steps need to be appropriately defined: (i) time stepping; (ii) normal fluxes on edges; (iii) quadrature rules; (iv) Riemann problem. We would like to stress here that the approach developed below does not add important computational complexities beyond what is done in standard two-dimensional FV codes.

Step (i) uses a first order explicit Euler time stepping scheme. To maintain a well-balanced scheme we use an adaptation of the approach of [5,8] and include the source terms in the flux. Then, the following FV equations are defined for each T_i:

$$\mathbf{U}_{h,i}^{k+1} = \mathbf{U}_{h,i}^{k} - \frac{\Delta t}{\mathcal{A}_{h,i}}\sum_{j=1}^{N_{\sigma(i)}}\ell_{h,ij}\left[\mathbf{F}_{h,ij}\left(\mathbf{U}_{h,i}^{k},\mathbf{U}_{h,j}^{k}\right)+\mathbf{S}_{h,ij}\left(\mathbf{U}_{h,i}^{k},\mathbf{U}_{h,j}^{k}\right)\right], \tag{3.5}$$

where $\mathbf{F}_{h,ij}$ is the numerical approximation of the edge-averaged normal flux $\mathbf{F}_{ij}$ at σ_{ij}, and $\mathbf{S}_{h,ij}$ is calculated so that $\sum_{j=1}^{N_{\sigma(i)}}\ell_{h,ij}\mathbf{S}_{h,ij}$ is a consistent quadrature rule for the last integral in equation (3.4) and maintains the discrete version of equation (2.21).

Step (ii) is defined as follows. Given a tangent plane $T_{\mathbf{M}_\sigma}\Gamma$ on the edge, with associated metric tensor $\mathcal{G}_{sw}$, and denoting by $\nu = \left[\nu^1,\nu^2\right]^T$ and $\tau = \left[\tau^1,\tau^2\right]^T$ the normal and tangent vectors to the geodesic edge, the normal flux function can be written as:

$$\mathbf{F}^{\nu}(\mathbf{s},\mathbf{U}) = \left\langle \underline{\underline{F}}, \nu\right\rangle_{\mathcal{G}} = \begin{bmatrix} q^1 h_{(1)}^2\nu^1 + q^2 h_{(2)}^2\nu^2 \\ \frac{\left(q^1\right)^2}{\eta}h_{(1)}^2\nu^1 + \frac{1}{2}g\eta^2\frac{\partial x^3}{\partial s^3}\nu^1 + \frac{q^1q^2}{\eta}h_{(2)}^2\nu^2 \\ \frac{q^1q^2}{\eta}h_{(1)}^2\nu^1 + \frac{\left(q^2\right)^2}{\eta}h_{(2)}^2\nu^2 + \frac{1}{2}g\eta^2\frac{\partial x^3}{\partial s^3}\nu^2 \end{bmatrix}. \tag{3.6}$$

Using an edge-based LCS aligned with the normal and tangent vectors, we can write:

$$\begin{aligned} q^N &= \langle\vec{q},\nu\rangle_{\mathcal{G}} = q^1h_{(1)}^2\nu^1 + q^2h_{(2)}^2\nu^2 \\ q^T &= \langle\vec{q},\tau\rangle_{\mathcal{G}} = q^1h_{(1)}^2\tau^1 + q^2h_{(2)}^2\tau^2 = -q^1h_{(1)}^2\nu^2 + q^2h_{(2)}^2\nu^1, \end{aligned}$$

where we have used the relation $\tau = \left[\tau^1,\tau^2\right]^T = \left[-\nu^2,\nu^1\right]^T$. Finally, the normal flux function in the edge LCS takes on the expression:

$$\mathbf{F}^{\nu}(\mathbf{s},\mathbf{U}) = \begin{bmatrix} q^N \\ \frac{q^1q^N}{\eta} + \frac{1}{2}g\eta^2\frac{\partial x^3}{\partial s^3}\nu^1 \\ \frac{q^2q^N}{\eta} + \frac{1}{2}g\eta^2\frac{\partial x^3}{\partial s^3}\nu^2 \end{bmatrix}.$$

The final two steps, (iii) and (iv), require the approximation of the relevant surface quantities and will be described in the next Sections 3.1 and 3.2.

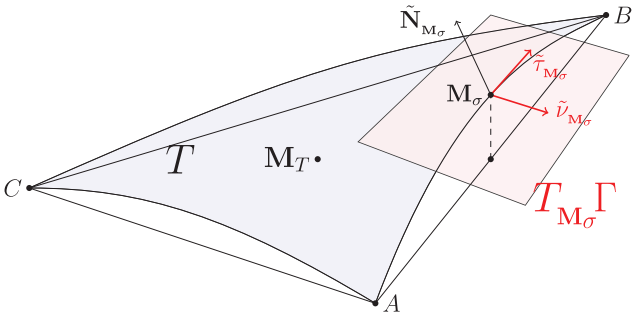

FIGURE 2. Curvilinear cell T and corresponding approximate gravity center $\mathbf{M}_T$. The curvilinear edge σ of cell T is the minimal geodesic curve connecting the two vertices. The midpoint of σ is denoted by $\mathbf{M}_\sigma$.

3.1. Intrinsic quadrature rules and sampling points

The aim is to define numerical quadrature rules consistent with the first order Godunov method we plan to use and with minimal sampling points. This will allow to solve a minimal number of Riemann problems per triangle edge. Linear consistency with a single sampling point is achieved by the midpoint formula, which can be written as:

$$\int_\sigma f(\mathbf{s})\,\mathrm{d}\sigma \approx \ell_\sigma f(\mathbf{M}_\sigma), \tag{3.7}$$

$$\int_T f(\mathbf{s})\,\mathrm{d}\mathbf{s} \approx \mathcal{A}_T f(\mathbf{M}_T), \tag{3.8}$$

where ℓ_σ is the length of the geodesic edge and $\mathcal{A}_T$ the area of the surface triangle, and $f(\mathbf{M}_\sigma)$ and $f(\mathbf{M}_T)$ denote the evaluation of the surface function at the edge and cell midpoints, respectively.

To address step (iii) we need to establish the approximations of the necessary geometric quantities. An important feature we want to maintain in our numerical approach is the exclusive use of geometrically intrinsic quantities. Up to this point, our FV scheme is defined intrinsically on the LCS attached on the bottom surface. To continue our development within this setting, we assume that all the relevant intrinsic information, namely the tangent plane, is known (in exact or approximate form) at the vertices of the triangulation. Then the task is to develop intrinsic approximations of the geometric quantities starting from these data.

Approximation on edges. With reference to Figure 2, we directly approximate the LCS (or equivalently the tangent plane) at the edge midpoint $\mathbf{M}_\sigma$ using nodal information, without actually resorting to an explicit expression for $\mathbf{M}_\sigma$. We start by approximating the tangent plane $T_{\mathbf{M}_\sigma}\Gamma$ from the linear interpolation of the tangent vectors $\mathbf{t}_i(A)$ and $\mathbf{t}_i(B)$, $i=1,2$, with re-orthogonalization. The frame completing normal vector is naturally obtained using the normalized outer product of $\tilde{\mathbf{t}}_i$. The three LCS vectors are thus given by:

$$\begin{aligned}
\tilde{\mathbf{t}}_1(\mathbf{M}_\sigma) &= \frac{1}{2}\mathbf{t}_1(A) + \frac{1}{2}\mathbf{t}_1(B),\\
\mathbf{t}_2'(\mathbf{M}_\sigma) &= \frac{1}{2}\mathbf{t}_2(A) + \frac{1}{2}\mathbf{t}_2(B), \quad \tilde{\mathbf{t}}_2(\mathbf{M}_\sigma) = \mathbf{t}_2' - \frac{\langle \mathbf{t}_2', \tilde{\mathbf{t}}_1\rangle}{\langle \tilde{\mathbf{t}}_1, \tilde{\mathbf{t}}_1\rangle}\tilde{\mathbf{t}}_1,\\
\tilde{\mathbf{t}}_3(\mathbf{M}_\sigma) &= \frac{\tilde{\mathbf{t}}_1 \wedge \tilde{\mathbf{t}}_2}{\|\tilde{\mathbf{t}}_1\|\,\|\tilde{\mathbf{t}}_2\|}.
\end{aligned}$$

The tangent plane at $\mathbf{M}_\sigma$ is then identified by $T_{\mathbf{M}_\sigma}\Gamma = \langle \tilde{\mathbf{t}}_1, \tilde{\mathbf{t}}_2 \rangle$, and the associated metric tensor is:

$$\tilde{\mathcal{G}}_{\mathbf{M}_\sigma} = \begin{bmatrix} \left\|\tilde{\mathbf{t}}_1\right\|^2 & 0 \\ 0 & \left\|\tilde{\mathbf{t}}_2\right\|^2 \end{bmatrix}.$$

Note that this approximation is fully intrinsic and does not require information on the geodesic edge between A and B.

The intrinsic definition of the Riemann problem requires the approximation of the normal and tangent directions to the geodesic edge at the midpoint. This is achieved as follows. The tangent plane is identified by its normal, given by:

$$\tilde{\mathbf{N}}_{\mathbf{M}_\sigma} = \tilde{\mathbf{t}}_3 \left(\mathbf{M}_\sigma\right).$$

The tangent vector is approximated by a second order accurate linear interpolation of the vectors tangent to the geodesic edge at the two vertices. Let $\sigma(\lambda)$ be a parametrization of the geodesic curve connecting the two nodes A and B and forming edge σ, with $\lambda \in [0,1]$ (see Fig. 2). In our case, we approximate this parametrization using the following expression:

$$\underline{\sigma}(\lambda) = \begin{cases} s^1(\lambda) = \left(s^1_B - s^1_A\right)\lambda + s^1_A \\ s^2(\lambda) = \left(s^2_B - s^2_A\right)\lambda + s^2_A \\ s^3(\lambda) = \mathcal{B}\left(s^1(\lambda),\, s^2(\lambda)\right), \end{cases} \tag{3.9}$$

where the third component of this parametric curve is the vertical projection of the chord onto the surface and not the real geodesic curve connecting A and B. Then, we compute the derivatives at the extremal points of this curve, obtaining the vectors tangent to the relevant edge at the triangle nodes, which in our case are:

$$\tau_A = \dot{\underline{\sigma}}(0), \quad \tau_B = \dot{\underline{\sigma}}(1).$$

The tangent vector at $\mathbf{M}_\sigma$ of the geodesic edge is then given by linear interpolation of τ_A and τ_B, orthogonalized with respect to the $\tilde{\mathbf{N}}_{\mathbf{M}_\sigma}$ to project it on $T_{\mathbf{M}_\sigma}\Gamma$:

$$\tau'_{\mathbf{M}_\sigma} = \frac{1}{2}\left(\tau_A + \tau_B\right), \quad \tilde{\tau}_{\mathbf{M}_\sigma} = \tau'_{\mathbf{M}_\sigma} - \frac{\left\langle \tau'_{\mathbf{M}_\sigma}, \tilde{\mathbf{N}}_{\mathbf{M}_\sigma} \right\rangle}{\left\langle \tilde{\mathbf{N}}_{\mathbf{M}_\sigma}, \tilde{\mathbf{N}}_{\mathbf{M}_\sigma} \right\rangle} \tilde{\mathbf{N}}_{\mathbf{M}_\sigma}.$$

Hence, the outer product of $\tilde{\tau}_{\mathbf{M}_\sigma}$ and $\tilde{\mathbf{N}}_{\mathbf{M}_\sigma}$ gives the approximation of the intrinsic normal to the geodesic edge, namely:

$$\tilde{\nu}_{\mathbf{M}_\sigma} = \tilde{\tau}_{\mathbf{M}_\sigma} \wedge \tilde{\mathbf{N}}_{\mathbf{M}_\sigma}. \tag{3.10}$$

To complete the definition we need to express $\tilde{\nu}_{\mathbf{M}_\sigma}$ and $\tilde{\tau}_{\mathbf{M}_\sigma}$ using the LCS bases. This provides the approximate vectors that define a proper rotation and projection in the direction orthogonal to the edge at the midpoint.

Approximation on cells. Analogous approximations need to be done in order to define the geometric information on the cells, namely the tangent plane at the gravity center of the cell $\mathbf{M}_T$. As before, we start from nodal data and construct the following vectors:

$$\begin{aligned} \tilde{\mathbf{t}}_1(\mathbf{M}_T) &= \frac{1}{3}\mathbf{t}_1(A) + \frac{1}{3}\mathbf{t}_1(B) + \frac{1}{3}\mathbf{t}_1(C), \\ \mathbf{t}'_2(\mathbf{M}_T) &= \frac{1}{3}\mathbf{t}_2(A) + \frac{1}{3}\mathbf{t}_2(B) + \frac{1}{3}\mathbf{t}_2(C), \quad \tilde{\mathbf{t}}_2(\mathbf{M}_T) = \mathbf{t}'_2 - \frac{\left\langle \mathbf{t}'_2, \tilde{\mathbf{t}}_1 \right\rangle}{\left\langle \tilde{\mathbf{t}}_1, \tilde{\mathbf{t}}_1 \right\rangle}\tilde{\mathbf{t}}_1, \\ \tilde{\mathbf{t}}_3(\mathbf{M}_T) &= \frac{\tilde{\mathbf{t}}_1 \wedge \tilde{\mathbf{t}}_2}{\left\|\tilde{\mathbf{t}}_1\right\| \left\|\tilde{\mathbf{t}}_2\right\|}, \end{aligned}$$

with the associated metric tensor

$$\tilde{\mathcal{G}}_{\mathbf{M}_T} = \begin{bmatrix} \left\|\tilde{\mathbf{t}}_1\right\|^2 & 0 \\ 0 & \left\|\tilde{\mathbf{t}}_2\right\|^2 \end{bmatrix}.$$

3.1.1. Approximation error estimates

In this paragraph we derive approximation error estimates for the quantities defined in the previous paragraph. In particular, we need to control the accuracy of the quadrature rule and, as a consequence, of the divergence theorem so that consistency of the IFV is ensured. In addition, the given estimates will relate these errors with the geometrical properties of the bottom surface. To this aim, we follow [28] and define the following quantities. Given $T \in \mathcal{T}(\Gamma)$ and $T_h \in \mathcal{T}_h(\Gamma)$ let $(m, \mathrm{pr}(m)) \in T_h \times T$ be the pair of points related by the orthogonal projection $\mathrm{pr}(m)$ with respect to $\xi = \mathbf{N}(\mathrm{pr}(m))$. Denote by $\|L_\xi(\mathrm{pr}(m))\|$ the norm of the Weingarten tensor, *i.e.*, the maximum of the absolute values of the principal curvatures of Γ along ξ in $\mathrm{pr}(m)$. Then, we can define the relative curvature function $\omega_\Gamma(m)$ of point m with respect to Γ as the product of the Euclidean distance $\left|\overrightarrow{\mathrm{pr}(m)m}\right|$ between $\mathrm{pr}(m)$ and m times $\|L_\xi(\mathrm{pr}(m))\|$, *i.e.*, $\omega_\Gamma(m) = \left|\overrightarrow{\mathrm{pr}(m)m}\right| \|L_\xi\|$. The relative curvature $\omega_\Gamma(U)$ of $U \subset \mathcal{T}_h(\Gamma)$ with respect to Γ is defined as $\omega_\Gamma(U) = \sup_{m\in U} \omega_\Gamma(m)$. In addition, we can define the deviation angle of $T_h \in \mathcal{T}_h$ with respect to $T \in \mathcal{T}$ as the maximum over all the points $m \in T_h$ of the angle $\alpha_{\max} \in [0, \pi/2]$ between the tangent space at $\mathrm{pr}(m)$ and T_h. Finally, we have the following proposition, which we state without proof (see [28]):

Proposition 3.1. *The following relations hold:*

(1) *the curvilinear length ℓ_σ of edge σ is related to the Euclidean length ℓ_{σ_h} via the inequalities:*

$$\ell_{\sigma_h} \le \ell_\sigma \le \frac{1}{1-\omega_\Gamma(\sigma_h)}\ell_{\sigma_h},$$

where $\omega_\Gamma(\sigma_h)$ is the relative curvature with respect to Γ;

(2) *the difference between the unit vector $\mathbf{v}_{\overline{AB}}$ aligned to the chord σ_h and the unit tangent vector τ_A to the geodesic edge at A satisfies:*

$$\left|\mathbf{v}_{\overline{AB}} - \tau_A\right| \le \frac{1}{2}k_\Gamma \ell_\sigma,$$

where k_Γ is the supremum over Γ of the norm of the second fundamental form;

(3) *the surface area of the cell T is related to the planar area of T_h by the relation:*

$$|\mathcal{A}_T - \mathcal{A}_{T_h}| \le C_\Gamma\left(\alpha_{\max}^2 + \omega_\Gamma(T_h)\right),$$

where C_Γ is a constant depending on Γ.

Remark 3.2. For any $U \subseteq T_h$ we have that for all $m \in U$ the length of the orthogonal projection $\overrightarrow{\mathrm{pr}(m)m}$ is bounded by the square of the length of the longest triangle edge, *i.e.*, $\left|\overrightarrow{\mathrm{pr}(m)m}\right| \le C\ell_{\sigma_h}^2$ [17]. From the definition of the relative curvature we find immediately $\omega_\Gamma(U) = \sup_{m\in U}\left|\overrightarrow{\mathrm{pr}(m)m}\right| \|L_\xi\| \le C\ell_{\sigma_h}^2$, where here C is a generic constant.

Remark 3.3. Analogously, the deviation angle $\alpha_{\max}$ of T_h with respect to T is bounded by the radius of the triangle circumcircle, leading to the bound $\alpha_{\max} \le C\ell_{\sigma_h}$ [28].

For a regular surface, the piecewise linear interpolant $I_h f$ of a smooth function is characterized by quadratic error [17]:

$$\|f - I_h f\|_{L^2(T)} \le C\ell_{\sigma_h}^2 \left\|D^2 f\right\|_{L^2(T)}.$$

In Section 4.1 we will show the experimental convergence results confirming this fact in our setting. Since we assume that the flux and source functions are Lipschitz regular, their evaluation at the sampling points maintains the order of accuracy. Thus, to complete our analysis, we are left with the study of the approximation errors introduced in the quadrature rules by the definition of the tangent/normal reference frame in $T_{\mathbf{M}_\sigma}\Gamma$. In

particular, we analyze here the quadrature rule for an integral over the edge σ of a general Lipschitz regular vector function F. Here we denote with $\tilde{F}^{\nu}(\mathbf{M}_\sigma)$ the evaluation of the function F on the approximate $T_{\mathbf{M}_\sigma}\Gamma$ at the edge midpoint $\mathbf{M}_\sigma$ projected along the approximate normal direction $\tilde{\nu}_{\mathbf{M}_\sigma}$. Then, we have the following result:

Proposition 3.4. *Given a Lipschitz regular vector function F defined on the geodesic edge σ we have:*

$$\int_\sigma \langle F, \nu \rangle_{\mathcal{G}} \, \mathrm{d}\sigma = \ell_{\sigma_h} \tilde{F}^{\nu}(\mathbf{M}_\sigma) + \mathcal{O}\big(\ell_{\sigma_h}^2\big) .$$

Proof. Direct application of the mid-point rule yields [20]:

$$\int_\sigma \langle F, \nu \rangle_{\mathcal{G}} \, \mathrm{d}\sigma = \ell_\sigma \langle F, \nu \rangle_{\mathcal{G}}(\mathbf{M}_\sigma) + \mathcal{O}\big(\ell_\sigma^3\big) .$$

Next we address explicitly the different approximations made in the definition of $T_{\mathbf{M}_\sigma}\Gamma$. We first note that, by Proposition 3.1 (2), we have:

$$|\tau - \tilde{\tau}_{\mathbf{M}_\sigma}| \leq \left|\tau - \mathbf{v}_{\overrightarrow{AB}}\right| + \left|\mathbf{v}_{\overrightarrow{AB}} - \tilde{\tau}_{\mathbf{M}_\sigma}\right| \leq C\ell_\sigma,$$

where C is a constant depending on the surface curvature. By construction, the approximate normal $\tilde{\nu}_{\mathbf{M}_\sigma}$ shares the same first order error estimate. Recalling Remark 3.2, essentially Proposition 3.1 (1) states that $|\ell_\sigma - \ell_{\sigma_h}| \leq C\ell_{\sigma_h}^3$. Linear interpolation of the nodal quantities ensures that the approximate metric and tangent plane in $\mathbf{M}_\sigma$ are second order accurate, *i.e.*:

$$\mathcal{G}(\mathbf{M}_\sigma) = \tilde{\mathcal{G}}_{\mathbf{M}_\sigma} + \mathcal{O}\big(\ell_\sigma^2\big) \quad \text{and} \quad F(\mathbf{M}_\sigma) = \tilde{F}(\mathbf{M}_\sigma) + \mathcal{O}\big(\ell_\sigma^2\big) .$$

Thus, expanding the scalar product $\langle \cdot, \cdot \rangle_{\mathcal{G}}$ and combining all the terms, we can write:

$$\begin{aligned}
\ell_\sigma \langle F, \nu \rangle_{\mathcal{G}}(\mathbf{M}_\sigma) + \mathcal{O}\big(\ell_\sigma^3\big) &= \ell_\sigma \Big(\tilde{F}(\mathbf{M}_\sigma) + \mathcal{O}\big(\ell_\sigma^2\big)\Big)\Big(\tilde{\mathcal{G}}_{\mathbf{M}_\sigma} + \mathcal{O}\big(\ell_\sigma^2\big)\Big)\left(\tilde{\nu}_{\mathbf{M}_\sigma} + \mathcal{O}(\ell_\sigma)\right) + \mathcal{O}\big(\ell_\sigma^3\big) \\
&= \ell_\sigma \Big(\tilde{F}(\mathbf{M}_\sigma)\, \tilde{\mathcal{G}}_{\mathbf{M}_\sigma} \tilde{\nu}_{\mathbf{M}_\sigma} + \mathcal{O}(\ell_\sigma)\Big) + \mathcal{O}\big(\ell_\sigma^3\big) \\
&= \ell_{\sigma_h} \tilde{F}^{\nu}(\mathbf{M}_\sigma) + \mathcal{O}\big(\ell_{\sigma_h}^2\big) ,
\end{aligned}$$

which yields the desired result. □

Because of its importance in our IFV scheme, we report here the following corollary whose proof is an immediate consequence of the previous proposition.

Corollary 3.5. *Given a Lipschitz regular vector function F defined on the geodesic triangle T we have:*

$$\int_T \nabla_{\mathcal{G}} \cdot F \, \mathrm{d}\mathbf{s} = \sum_{j=1}^{N_\sigma} \ell_{h,j} \tilde{F}^{\nu}\left(\mathbf{M}_{\sigma_j}\right) + \mathcal{O}\big(\ell_{\sigma_h}^2\big) .$$

We end this section by noting that all these estimates can be directly related to the global mesh parameter h. This is classically defined as the maximum of the lengths of the triangulation edges, *i.e.*, $h = \max_{\sigma_h \in \mathcal{T}_h(\Gamma)} \ell_{\sigma_h}$. Noting that, by Remarks 3.2 and 3.3 and Proposition 3.1 (3), the area of T_h converges quadratically to the area of T, we can conclude that all our geometric approximations involved in the calculation of the right-hand-side of equation (3.5) are consistent with the global accuracy of our IFV discretization.

3.2. The Riemann problem

As customary in upwind-Godunov methods, the numerical fluxes $\mathbf{F}_{h,ij}$ in equation (3.5) are defined by evaluating the flux function $\mathbf{F}^{\nu}_{ij}$ from solutions of Riemann Problems (RPs) at quadrature points of the cell edges. Since our equations are invariant under linear transformations and, specifically, rotations, each RP can be formulated as a one-dimensional problem in the tangent plane $T_{\mathbf{M}_\sigma}\Gamma$, passing through the quadrature point $\mathbf{M}_\sigma$ in the direction of the local edge normal $\tilde{\nu}_{\mathbf{M}_\sigma}$.

Note that our flux function is non-autonomous as it depends on the space variable defined on the local coordinate system. In this case difficulties in the well-posedness of the RP may arise (see *e.g.*, [2–4]). Thus, we write the Riemann problem as follows. Let $\mathbf{V} = \left[\eta, q^N, q^T\right]^T = \left[\eta, \eta v^1, \eta v^2\right]^T$ be the vector of conservative variables, where, q^N and q^T indicate the components of the flux (discharge) vector defined along the directions $\tilde{\nu}_{\mathbf{M}_\sigma}$ and $\tilde{\tau}_{\mathbf{M}_\sigma}$, respectively. Denote with x the space variable along $\tilde{\nu}_{\mathbf{M}_\sigma}$. Then, the RP is formally given by:

$$\begin{aligned}
&\mathbf{V}_t + \mathbf{F}^{\nu}\left(x, \mathbf{V}\right)_x = 0,\\
&\mathbf{F}^{\nu} : (x, \mathbf{V}) \in \Gamma \times T_{\mathbf{M}_\sigma}\Gamma \;\mapsto\; \begin{cases} \mathbf{F}_L\left(\mathbf{V}\right) & \text{if} \quad x < 0 \\ \mathbf{F}_R\left(\mathbf{V}\right) & \text{if} \quad x > 0 \end{cases},\\
&\mathbf{V}\left(x, 0\right) = \begin{cases} \mathbf{V}_L & \text{if} \quad x < 0 \\ \mathbf{V}_R & \text{if} \quad x > 0 \end{cases},
\end{aligned} \tag{3.11}$$

where $\mathbf{F}^{\nu}$ is the normal flux function as defined in equation (3.6). To simplify the problem, we advocate the assumption of continuity of the flux function with respect to the first argument. This allows us to approximate the RP by assuming $\mathbf{F}_L\left(\mathbf{V}\right) = \mathbf{F}_R\left(\mathbf{V}\right)$, thus recovering the standard form of the shallow-water RP. This approximation deserves further investigation, which is however outside the scope of this paper and we leave it to future studies.

Consistently with the first order accuracy, we use cell values to define the left and right initial states $\mathbf{V}_L$ and $\mathbf{V}_R$. However, the physical quantities of depth and velocity need to be written in the correct reference system attached on the edge midpoint. For each cell, η represents the cell average of the water column (measured in the normal direction) at the cell midpoint $\mathbf{M}_T$. Since we consider a surface triangulation, the midpoint of the cell can have a different elevation with respect to the GCS than the midpoint of the edge. Thus, the depth value needs to be properly moved to the point $\mathbf{M}_\sigma$, where the RP is defined. For edge σ, we calculate the left and right edge elevations $\eta_{(L)}$ and $\eta_{(R)}$ from the cell elevations η_L and η_R of cells T_L and T_R as follows:

$$\eta_{(k)} = \max\left\{0, \frac{\eta_k \left.\frac{\partial x^3}{\partial s^3}\right|_k + x^3_{\mathcal{B},k} - x^3_{\mathcal{B},\sigma}}{\left.\frac{\partial x^3}{\partial s^3}\right|_\sigma}\right\} \quad k = L, R,$$

where $\left.\frac{\partial x^3}{\partial s^3}\right|_k$ and $x^3_{\mathcal{B},k}$ are defined at the gravity center of the kth cell. The zero bound is introduced to ensure non-negativity of water depth. We need to define the edge-quantities $\left.\frac{\partial x^3}{\partial s^3}\right|_\sigma$ and $x^3_{\mathcal{B},\sigma}$. Because of the regularity of the bottom surface, we can set $\left.\frac{\partial x^3}{\partial s^3}\right|_\sigma = \frac{\partial x^3}{\partial s^3}\left(\mathbf{M}_\sigma\right)$. Definition of the edge bottom elevation $x^3_{\mathcal{B},\sigma}$ must take into consideration the fact that the edge might be in a dry region (*i.e.*, the edge midpoint is at a higher elevation with respect to the cell water elevation). Following [5, 8], we then set

$$x^3_{\mathcal{B},\sigma} = \max\left\{x^3_{\mathcal{B},L}, x^3_{\mathcal{B},R}, x^3_{\mathcal{B}}\left(\mathbf{M}_\sigma\right)\right\},$$

where $x^3_{\mathcal{B}}\left(\mathbf{M}_\sigma\right)$ is the approximated value at the edge center $\mathbf{M}_\sigma$. This ensures that dry regions with $\eta = 0$ are captured so that wetting-and-drying processes are handled seamlessly.

Concerning the velocity, the vector $\mathbf{q}$ must be "parallel" transported from the cell gravity center to the edge midpoint, so that all quantities in the RP belong to $T_{\mathrm{M}_\sigma}\Gamma$. This is achieved by a first order linearization of the ODE system defining parallel transport. Again, for edge σ we can write [18,32]:

$$q^1{}_{(k)}\left(\mathbf{s}_{\mathrm{M}_\sigma}\right) = q^1(\mathbf{s}_k) - \left(s^1_{\mathrm{M}_T} - s^1_k\right)\left(\Gamma^{1,(k)}_{11} q^1(\mathbf{s}_k) + \Gamma^{1,(k)}_{21} q^2(\mathbf{s}_k)\right) \qquad k = L, R. \tag{3.12a}$$

$$q^2{}_{(k)}\left(\mathbf{s}_{\mathrm{M}_\sigma}\right) = q^2(\mathbf{s}_k) - \left(s^2_{\mathrm{M}_T} - s^2_k\right)\left(\Gamma^{2,(k)}_{11} q^1(\mathbf{s}_k) + \Gamma^{2,(k)}_{21} q^2(\mathbf{s}_k)\right) \tag{3.12b}$$

Note that this first order linearization maintains the accuracy of the overall scheme. However, its most important role is to perform the change of coordinate systems from the cell-attached to the edge-attached tangent planes.

3.2.1. The Riemann solver

We use the classical HLL and its variant HLLC schemes [22,37], which easily adapt to our equations. The HLL scheme estimates the smallest and largest wave speeds S_L, S_R in the solution of the Riemann problem starting from the left and right data $\mathbf{U}_L, \mathbf{U}_R$ defined in the neighboring cells to the edge and the corresponding fluxes $\mathbf{F}_L = \mathbf{F}^\nu(\mathbf{V}_L)$ and $\mathbf{F}_R = \mathbf{F}^\nu(\mathbf{V}_R)$. It is easy to calculate the extremal eigenvalues of the Jacobian as:

$$S_L = \min\left\{0,\ \min\left\{\mathbf{v}_L - \sqrt{g\eta_L \frac{\partial x^3}{\partial s^3}\Big|_L},\ \mathbf{v}_R - \sqrt{g\eta_R \frac{\partial x^3}{\partial s^3}\Big|_R}\right\}\right\},$$

$$S_R = \max\left\{0,\ \max\left\{\mathbf{v}_L + \sqrt{g\eta_L \frac{\partial x^3}{\partial s^3}\Big|_L},\ \mathbf{v}_R + \sqrt{g\eta_R \frac{\partial x^3}{\partial s^3}\Big|_R}\right\}\right\}.$$

Considering the normal direction defined in equation (3.11), the HLL flux on the edge is then computed as:

$$\mathbf{F}^\nu_{HLL} = \begin{cases} \mathbf{F}_L & \text{if} \quad S_L \geq 0 \\ \dfrac{S_R\mathbf{F}_L - S_L\mathbf{F}_R + S_R S_L\left(\mathbf{U}_R - \mathbf{U}_L\right)}{S_R - S_L} & \text{if} \quad S_L \leq 0 \leq S_R \\ \mathbf{F}_R & \text{if} \quad S_R \leq 0. \end{cases} \tag{3.13}$$

Note that, this approach ignores intermediate waves, such as shear waves and contact discontinuities. Consideration of these waves is achieved in the HLLC approach described in [37], whose extension to our setting is straightforward.

3.2.2. The CFL condition

The knowledge of the eigenstructure of the Jacobian of the system is necessary also to enforce the stability condition, since we are applying an explicit time discretization method. The time step Δt follows from a standard CFL condition, where:

$$\mathrm{CFL} = \frac{\Delta t\, S_{\max}}{h_T},$$

with $S_{\max} = \left\|\vec{U}\right\|_{\mathcal{G}} + \sqrt{g\eta\frac{\partial x^3}{\partial s^3}}$. We typically impose that CFL be smaller than $1/2$ to ensure stability, and the actual time step is chosen as the minimum value over all the cells $T \in \mathcal{T}(\Gamma)$.

3.3. Well-balance

We look here at the well-balance property for the "lake-at-rest" condition. In this case, we have a steady-state condition with zero velocity and thus a time-independent horizontal free surface. Our intrinsic SW equation then becomes:

$$\begin{cases} \vec{q} = 0 \\ \nabla_{\mathcal{G}} \cdot \left(\frac{1}{2} g\eta^2 \dfrac{\partial x^3}{\partial s^3} \mathcal{G}^{-1}_{sw}\right) = -\frac{1}{2} g\eta^2\, \nabla_{\mathcal{G}} \dfrac{\partial x^3}{\partial s^3} - g\eta\, \nabla_{\mathcal{G}}\, x^3_{\mathcal{B}}, \end{cases}$$

which is equivalent to equation (2.21). We would like to note that more accurate well-balance properties would be needed in case of higher order methods, but in this paper we content ourselves with simple well-balance property in the form of the "lake-at-rest". We will consider as future studies the more complex situation of a fully well balanced scheme as done in [6, 7]. The divergence theorem can be used to express the cell-integral of the source term as a sum of integrals on the edges. In fact, from the steady momentum conservation equation we can write the following equalities:

$$\begin{aligned}\int_{T_i}\left(\frac{1}{2}g\eta^2\nabla_{\mathcal{G}}\frac{\partial x^3}{\partial s^3}+g\eta\nabla_{\mathcal{G}}x^3_{\mathcal{B}}\right)\mathrm{d}\mathbf{s} &= -\int_{T_i}\nabla_{\mathcal{G}}\cdot\left(\frac{1}{2}g\eta^2\frac{\partial x^3}{\partial s^3}\mathcal{G}^{-1}_{sw}\right)\mathrm{d}\mathbf{s}\\ &= -\sum_{j=1}^{3}\int_{\sigma_{ij}}\left\langle\frac{1}{2}g\eta^2\frac{\partial x^3}{\partial s^3}\mathcal{G}^{-1}_{sw},\nu_{ij}\right\rangle_{\mathcal{G}}\mathrm{d}\sigma\approx-\sum_{j=1}^{3}\ell_{h,ij}\left\langle\frac{1}{2}g\left(\eta^*_{ij}\right)^2\frac{\partial x^3}{\partial s^3}\Big|^*_{ij}\mathcal{G}^{-1}_{sw},\nu_{ij}\right\rangle_{\mathcal{G}},\end{aligned}\tag{3.14}$$

where the starred quantities are evaluated at appropriate sampling points so that discrete well-balance is maintained. Then, using the full expression of $\mathbf{S}(\mathbf{s},\eta)$, the integral over T_i can be written as:

$$\begin{aligned}\int_{T_i}\mathbf{S}\,\mathrm{d}\mathbf{s}&\approx\begin{bmatrix}0\\-\sum_{j=1}^{3}\ell_{h,ij}\left\langle\frac{1}{2}g\left(\eta^*_{ij}\right)^2\frac{\partial x^3}{\partial s^3}\Big|^*_{ij}\mathcal{G}^{-1}_{sw},\nu_{ij}\right\rangle_{\mathcal{G}}\end{bmatrix}\\&=\sum_{j=1}^{3}\ell_{h,ij}\begin{bmatrix}0\\-\left\langle\frac{1}{2}g\left(\eta^*_{ij}\right)^2\frac{\partial x^3}{\partial s^3}\Big|^*_{ij}\mathcal{G}^{-1}_{sw},\nu_{ij}\right\rangle_{\mathcal{G}}\end{bmatrix}=\sum_{j=1}^{3}\ell_{h,ij}\begin{bmatrix}0\\\mathbf{S}_{ij}\end{bmatrix}.\end{aligned}$$

The idea is to apply the latter relation as a quadrature rule for the source integral in the scheme also in the non steady-state case. This quadrature rule is, by definition, exact when the velocity is zero and we need to prove that its approximation error is of order $\mathcal{O}(h)$ when the velocity is non-zero. Moreover, it has to be consistent with the flux term $\mathbf{F}_{ij}$ computed *via* Riemann solvers.

We first define the sampling values η^*_{ij} and $\frac{\partial x^3}{\partial s^3}\Big|^*_{ij}$ used in $\mathbf{S}_{ij}$ that ensure well-balance and consistency, with the first condition satisfied exactly. In the case of a steady horizontal water table, discrete well-balance implies that, with respect to the GCS, the total water elevation at the cell-center must equal the total water elevation at the edge center:

$$\eta_i\frac{\partial x^3}{\partial s^3}\Big|_i+x^3_{\mathcal{B},i}=\eta_{ij}\frac{\partial x^3}{\partial s^3}\Big|_{ij}+x^3_{\mathcal{B},ij},\tag{3.15}$$

which yields immediately:

$$\eta_{ij}=\frac{\eta_i\frac{\partial x^3}{\partial s^3}\Big|_i+x^3_{\mathcal{B},i}-x^3_{\mathcal{B},ij}}{\frac{\partial x^3}{\partial s^3}\Big|_{ij}},\tag{3.16}$$

where we define the values at the edge as described in Section 3.2. Then, we ensure non-negativity of water depth by defining $\eta^*_{ij}=\max\{0,\eta_{ij}\}$. We then have the following proposition.

Proposition 3.6. *The intrinsic finite volume scheme (3.5) (i) preserves the non-negativity of η_i; (ii) is well-balanced, i.e., preserves the steady-state of a lake-at-rest (Eq. (3.15)); (iii) is consistent with the continuous ISWE model (Eq. (2.18)).*

Proof. Statement (i) follows directly from the definition of η^*_{ij}, which ensures $0\le\eta^*_{ij}\le\eta_i$ and $0\le\eta^*_{ji}\le\eta_j$.

Property (ii) of steady-state for lake-at-rest is maintained by the consistency of the flux $\mathbf{F}_{ij}$, valid by construction, and the definition of the source terms at the interface.

To prove Property (iii) we need to establish the consistency of the scheme for the general case of a nonzero velocity, *i.e.*, $\vec{q} \neq 0$. To this aim it is sufficient to prove that the left and right fluxes for edge σ_{ij}, $\mathcal{F}_L = \mathbf{F}_{ij} + \mathbf{S}_{ij}$ and $\mathcal{F}_R = \mathbf{F}_{ji} + \mathbf{S}_{ji}$, respectively, satisfy the following condition [8]:

$$\mathcal{F}_L + \mathcal{F}_R = \mathbf{f}(\eta)\ h + o(h)\,, \tag{3.17}$$

where $\mathbf{f}(\eta)$ indicates a general vector function of the depth only, and $o(\cdot)$ is used as in the standard little-o notation. Obviously, our numerical flux $\mathbf{F}_{ij}$ is consistent:

$$\mathbf{F}_{ij} = \left\langle \underline{\underline{F}}(\mathbf{U}^*), \nu_{ij} \right\rangle_{\mathcal{G}} = \left\langle \underline{\underline{F}}(\mathbf{U}^*), -\nu_{ji} \right\rangle_{\mathcal{G}} = -\mathbf{F}_{ji}.$$

It remains to show the consistency for the edge source terms, that are nonzero only for the two momentum conservation equations. Recall that, due to the assumption of regularity of the bottom surface $\mathcal{S}_{\mathcal{B}}$, Taylor expansions for functions living on Γ are well defined (see [16]). Moreover, for a general surface vector $\mathbf{v}$ written in physical coordinates and a scalar function f we can write $\langle \nabla_{\mathcal{G}} f, \mathbf{v} \rangle_{\mathcal{G}} = \langle \nabla f, \mathbf{v} \rangle$. Hence we have:

$$\begin{aligned}
x^3_{\mathcal{B},ij} &= x^3_{\mathcal{B},i} + \nabla x^3_{\mathcal{B},i} \cdot (\mathbf{s}_{ij} - \mathbf{s}_i) + o(h)\,, \\
\left.\frac{\partial x^3}{\partial s^3}\right|_{ij} &= \left.\frac{\partial x^3}{\partial s^3}\right|_{i} + \nabla \left(\left.\frac{\partial x^3}{\partial s^3}\right|_{i} \right) \cdot (\mathbf{s}_{ij} - \mathbf{s}_i) + o(h)\,, \\
\eta_{ij} &= \eta_i + \nabla \eta_i \cdot (\mathbf{s}_{ij} - \mathbf{s}_i) + o(h)\,,
\end{aligned}$$

where $\mathbf{s}_{ij}, \mathbf{s}_i$ are the LCS coordinates of $\mathbf{M}_{\sigma_{ij}}$ and $\mathbf{M}_{T_i}$, respectively, and we have used the fact that $|\mathbf{s}_{ij} - \mathbf{s}_i| = \mathcal{O}(h)$. Analogously, from equation (3.16), we can write:

$$\eta^*_{ij} \left.\frac{\partial x^3}{\partial s^3}\right|^*_{ij} = \eta_i \left.\frac{\partial x^3}{\partial s^3}\right|_{i} + x^3_{\mathcal{B},i} - x^3_{\mathcal{B},ij} = \eta_i \left.\frac{\partial x^3}{\partial s^3}\right|_{i} + \nabla x^3_{\mathcal{B},i} \cdot (\mathbf{s}_{ij} - \mathbf{s}_i) + o(h)\,.$$

From Corollary 3.5, applying the divergence theorem to the constant vectors $[1, 0]$ and $[0, 1]$ we obtain:

$$0 = \int_{\partial T_i} \nu \, \mathrm{d}\sigma = \sum_{j=1}^{3} \ell_{h,ij} \nu_{ij} + \mathcal{O}(h^2)\,.$$

Thus, we add to the edge-evaluated source a term that, when summed over all the cell edges, gives a $\mathcal{O}(h^2)$ contribution:

$$\mathbf{S}^{\vec{q}}_{ij} = \left\langle \frac{1}{2} g \left(\eta^*_{ij}\right)^2 \left.\frac{\partial x^3}{\partial s^3}\right|^*_{ij} \mathcal{G}^{-1}_{sw}, \nu_{ij} \right\rangle_{\mathcal{G}} - \left\langle \frac{1}{2} g \eta_i^2 \left.\frac{\partial x^3}{\partial s^3}\right|_{i} \mathcal{G}^{-1}_{sw}, \nu_{ij} \right\rangle_{\mathcal{G}} + \mathcal{O}(h^2)\,.$$

Then we can write:

$$\begin{aligned}
\mathbf{S}^{\vec{q}}_{ij} + \mathbf{S}^{\vec{q}}_{ji} = &\left\langle \frac{1}{2} g \left[\left(\eta^*_{ij}\right)^2 \left.\frac{\partial x^3}{\partial s^3}\right|^*_{ij} - \eta_i^2 \left.\frac{\partial x^3}{\partial s^3}\right|_{i} \right] \mathcal{G}^{-1}_{sw}, \nu_{ij} \right\rangle_{\mathcal{G}} \\
&+ \left\langle \frac{1}{2} g \left[\left(\eta^*_{ji}\right)^2 \left.\frac{\partial x^3}{\partial s^3}\right|^*_{ji} - \eta_j^2 \left.\frac{\partial x^3}{\partial s^3}\right|_{j} \right] \mathcal{G}^{-1}_{sw}, \nu_{ji} \right\rangle_{\mathcal{G}} + \mathcal{O}(h^2) \\
= &\left\langle \frac{1}{2} g \left[\left(\eta^*_{ij}\right)^2 \left.\frac{\partial x^3}{\partial s^3}\right|^*_{ij} - \eta_i^2 \left.\frac{\partial x^3}{\partial s^3}\right|_{i} - \left(\eta^*_{ji}\right)^2 \left.\frac{\partial x^3}{\partial s^3}\right|^*_{ji} + \eta_j^2 \left.\frac{\partial x^3}{\partial s^3}\right|_{j} \right] \mathcal{G}^{-1}_{sw}, \nu_{ij} \right\rangle_{\mathcal{G}} + \mathcal{O}(h^2)\,.
\end{aligned} \tag{3.18}$$

Substituting the Taylor expansions written above, the term within the square brackets becomes:

$$
\begin{aligned}
&\left[\eta^*_{ij}\left(\eta_i\frac{\partial x^3}{\partial s^3}\Big|_i+\nabla x^3_{\mathcal{B},i}\cdot(\mathbf{s}_{ij}-\mathbf{s}_i)\right)-\eta_i^2\frac{\partial x^3}{\partial s^3}\Big|_i\right]\\
&\quad-\left[\eta^*_{ji}\left(\eta_j\frac{\partial x^3}{\partial s^3}\Big|_j+\nabla x^3_{\mathcal{B},j}\cdot(\mathbf{s}_{ji}-\mathbf{s}_j)\right)-\eta_j^2\frac{\partial x^3}{\partial s^3}\Big|_j\right]+\mathcal{O}(h^2)\\
&=(\eta_i+\nabla\eta_i\cdot(\mathbf{s}_{ij}-\mathbf{s}_i))\left(\eta_i\frac{\partial x^3}{\partial s^3}\Big|_i+\nabla x^3_{\mathcal{B},i}\cdot(\mathbf{s}_{ij}-\mathbf{s}_i)\right)-\eta_i^2\frac{\partial x^3}{\partial s^3}\Big|_i\\
&\quad-(\eta_j+\nabla\eta_j\cdot(\mathbf{s}_{ji}-\mathbf{s}_j))\left(\eta_j\frac{\partial x^3}{\partial s^3}\Big|_j+\nabla x^3_{\mathcal{B},j}\cdot(\mathbf{s}_{ji}-\mathbf{s}_j)\right)+\eta_j^2\frac{\partial x^3}{\partial s^3}\Big|_j+\mathcal{O}(h^2)\\
&=\left(\eta_i\nabla x^3_{\mathcal{B},i}+\eta_i\frac{\partial x^3}{\partial s^3}\Big|_i\nabla\eta_i\right)\cdot(\mathbf{s}_{ij}-\mathbf{s}_i)-\left(\eta_j\nabla x^3_{\mathcal{B},j}+\eta_j\frac{\partial x^3}{\partial s^3}\Big|_j\nabla\eta_j\right)\cdot(\mathbf{s}_{ji}-\mathbf{s}_j)\\
&\quad+\nabla\eta_i\cdot(\mathbf{s}_{ij}-\mathbf{s}_i)\nabla x^3_{\mathcal{B},i}\cdot(\mathbf{s}_{ij}-\mathbf{s}_i)-\nabla\eta_j\cdot(\mathbf{s}_{ji}-\mathbf{s}_j)\nabla x^3_{\mathcal{B},j}\cdot(\mathbf{s}_{ji}-\mathbf{s}_j)+\mathcal{O}(h^2),
\end{aligned}
$$

which, once inserted in equation (3.18), proves equation (3.17). □

3.4. Boundary conditions

The implementation of boundary conditions in our FV is obtained by specifying the appropriate edge value to the Riemann solver. In practice, on a boundary edge σ we define an outer $\mathbf{U}^{\text{out}}_\sigma$ and an inner $\mathbf{U}^{\text{in}}_\sigma$ state that form, depending on the direction of the local edge normal $\tilde{\nu}_{\mathcal{M}_\sigma}$, the left and right states for the edge Riemann solver. The boundary value $\mathbf{U}^{\text{out}}_\sigma$ is assumed to be given directly with respect of the reference system in the tangent plane $T_{\mathcal{M}_\sigma}\Gamma$, while internal values $\mathbf{U}^{\text{in}}_\sigma$ are defined on edge σ by parallel transport (3.12). In practice, following [36], we implemented two types of boundary conditions: transmissive boundaries and solid reflective boundaries. Transmissive boundaries are given by:

$$\eta^{\text{out}}=\eta^{\text{in}},\quad \mathbf{q}^{\text{out}}=\mathbf{q}^{\text{in}},$$

while, solid reflective boundaries are imposed by setting:

$$\eta^{\text{out}}=\eta^{\text{in}},\quad \mathbf{q}^{\text{out}}=-\mathbf{q}^{\text{in}},$$

where $\eta^{\text{in}},\mathbf{q}^{\text{in}}$ are the state values in the internal cell. Other more complex types of boundary conditions, such those presented in [35], require adaptation to our setting and are not considered here.

4. Numerical results

Our numerical tests are designed to experimentally verify the applicability of the developed scheme to the simulation of the SWE on surfaces. Specifically, we want to test selected properties of the obtained numerical solution showing the robustness of the proposed approach. To this aim, we first show convergence of the discretization of the geometric quantities on smooth surfaces, then look at experimental convergence on full scale realistic tests.

The design of the test cases needs to be aware of the assumption underlying our continuous formulation and the discretization approach. All the test cases simulate a gravity-driven fluid in a dam-break setting, without any stress tensor. The initial conditions are defined to initiate a dam-break phenomenon, with water depth in any case small enough to exclude the issue of the intersection of the local normals so that the coordinate transformation is always a diffeomorphism. Different initial conditions on water depth are considered depending on the shape of the bottom surface, while we always consider zero initial velocities. No-flow boundary conditions are imposed everywhere except at the outlet boundary, where a free outflow is enforced. The value of the time step Δt is calculated so that CFL $\approx$ 0.1. We choose a triangulation of the domain that is aligned with three

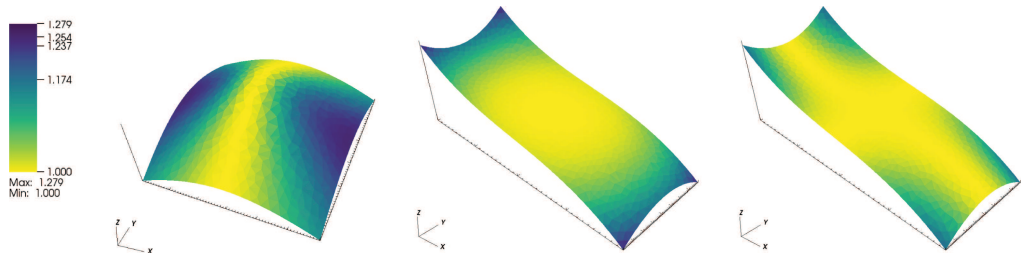

FIGURE 3. Spatial distribution of the metric coefficients $h_{(1)}$ for the hyperboloid-central-bump (*left*) and of $h_{(i)}$, $i = 1, 2$, for the Fully 3D surface (*center* and *right*).

straight cross-sections uniformly distributed across the main flow directions that are used to evaluate streamflows (*i.e.*, discharge *vs.* time).

Since no analytical solution is available for the case of variable bottom geometry if not for simple cases (*i.e.*, planar free surface [15]), we investigate numerical stability and convergence by looking at errors calculated as differences with a fine-grid solution, assumed as reference solution. We look at L^1- and L^2-error norms and calculate the experimental order of convergence.

For all the bottom surfaces $\mathcal{S}_{\mathcal{B}}$, we use a global parametrization $x^3 = \mathcal{B}(x^1, x^2)$, with $\mathcal{B}$ a sufficiently smooth height function, whereby we start from a regular triangulation of a rectangular subset $U \subset \mathbb{R}^2$ and move the nodes vertically on Γ. In all cases, we assume that all relevant quantities of the bottom surface are known or can be approximated at the nodes of the triangulation, and use interpolation to define needed quantities at other points, as described in the previous section. All the dimensional quantities are expressed in SI units.

We first consider a simple one-dimensional domain with simple one-dimensional curvature. Let U be the subset $[0, 10] \times [0, 1] \subset \mathbb{R}^2$ in a global reference frame, we use a height function that parameterizes a parabola and as given by:

$$\mathcal{B}(x^1, x^2) = \frac{1}{25}\left(x^1 - 10\right)^2.$$

This case aims at verifying the effect of the curvatures in a simple one-dimensional flow, with metric coefficients that are different from one and vary along x^1.

Then, we consider a centrally symmetric surface starting from a subset $U = [-3, 3] \times [-3, 3] \subset \mathbb{R}^2$ and a height function given by:

$$\mathcal{B}(x^1, x^2) = -\frac{4}{5}\sqrt{\left(x^1\right)^2 + \left(x^2\right)^2 + 1}. \tag{4.1}$$

This test case is a complete three-dimensional benchmark. Figure 3 (*left*), shows the geometry of the bottom surface, named for simplicity hyperboloid-central-bump (HCB), and the spatial distribution of the metric coefficient in the s^1-direction, the s^2-distribution being analogous and thus not shown.

Finally, we examine a more realistic fully three-dimensional bottom topography taken from [18] defined on the subset $U = [-10, 10] \times [-4, 4] \subset \mathbb{R}^2$ with height function expressed as:

$$\mathcal{B}(x^1, x^2) = -\frac{1}{500}\left(x^1\right)^3 - \frac{1}{100}x^1\left(x^2\right)^2.$$

In this case the bottom topography presents different curvature values in the two directions (Fig. 3, center and right) and varying characteristics that influence the flow dynamics.

4.1. Convergence of the surface quantities

In this section we verify the accuracy of the proposed approximation to the needed surface quantities. Thus, we look at the L^∞- and L^2-norms of the difference between the approximated values and exact values at the

TABLE 1. L^∞ and L^2 norms of the experimental errors on cells and order of convergence of the approximations to the bottom geometric quantities for the HCB surface.

	$x^3_{\mathcal{B}}$				$\frac{\partial x^3}{\partial s^3}$			
h_ℓ	ε_{L^∞}	eoc_ℓ	ε_{L^2}	eoc_ℓ	ε_{L^∞}	eoc_ℓ	ε_{L^2}	eoc_ℓ
0.668	4.38E−02		9.10E−02		1.20E−02		2.43E−02	
0.334	1.17E−02	1.906	2.29E−02	1.989	3.72E−03	1.691	6.22E−03	1.961
0.167	3.05E−03	1.932	5.73E−03	1.996	9.71E−04	1.936	1.57E−03	1.989
0.0834	7.81E−04	1.965	1.43E−03	1.999	2.45E−04	1.987	3.92E−04	1.997
0.0417	1.97E−04	1.984	3.58E−04	2.000	6.10E−05	2.003	9.80E−05	1.999
0.0208	4.96E−05	1.993	8.96E−05	2.000	1.53E−05	2.000	2.45E−05	2.000
	$\frac{\partial x^3}{\partial s^1}$				$\frac{\partial}{\partial s^1}\left(\frac{\partial x^3}{\partial s^3}\right)$			
0.668	2.68E−02		4.00E−02		6.07E−02		4.29E−02	
0.334	7.35E−03	1.862	1.02E−02	1.965	1.82E−02	1.735	1.08E−03	1.981
0.167	1.93E−03	1.930	2.57E−03	1.989	5.11E−03	1.833	2.78E−03	1.964
0.0834	4.88E−04	1.983	6.44E−04	1.997	1.29E−03	1.983	6.99E−04	1.989
0.0417	1.23E−04	1.986	1.61E−04	1.999	3.27E−04	1.984	1.75E−04	1.997
0.0208	3.09E−05	1.994	4.03E−05	2.000	8.18E−05	1.997	4.38E−05	1.999

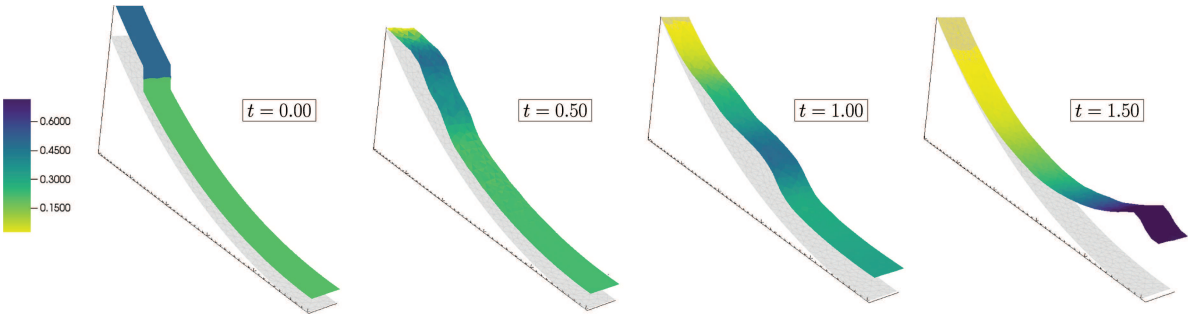

FIGURE 4. Parabola case: evolution of the gravity wave, shown both as color codes and depth elevation, the latter with a vertical magnification factor of 2.0.

gravity centers of cells and edges, respectively. Given the errors $\varepsilon(h_\ell)$ and $\varepsilon(h_{\ell+1})$ at grid levels ℓ and $\ell+1$, respectively, we calculate the experimental order of convergence eoc_ℓ. In particular, we look at the approximation errors to some of the geometric information that enter the SW system as approximated in the FV approach, namely bottom elevation $x^3_{\mathcal{B}}$, tangent vectors $\frac{\partial x^3}{\partial s^3}$ and $\frac{\partial x^3}{\partial s^1}$, and their derivative $\frac{\partial}{\partial s^1}\left(\frac{\partial x^3}{\partial s^3}\right)$. We look at these statistics for the HCB surface shown in Figure 3. The numerical results are shown in Table 1 and invariably show second order of convergence both on cell centers and edge midpoints, in agreement with the theoretical results described in the previous section.

4.2. Test case 1: parabola case

The parabola test case considers a simple one-dimensional flow where the effects of curvature in the model can be verified. We run our simulations on a grid with average mesh parameter $h = 0.26\,\mathrm{m}$, giving a total of 588 FV cells. We simulate the breaking of a dam located at $x^1 = 2.0\,\mathrm{m}$, with initially zero velocity everywhere and water depth of 0.5 m upstream and 0.2 m downstream the dam. We use the HLL Riemann solver, but no differences are noted with respect to the HLLC RS. Figure 4 shows the calculated distribution of the water depth η at times

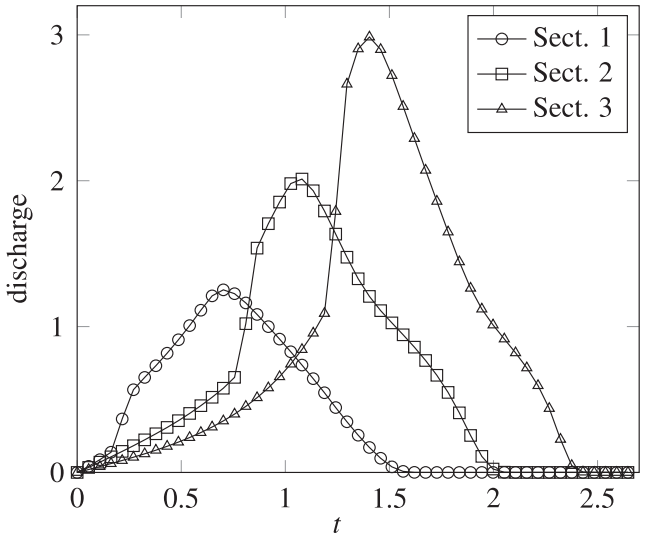

FIGURE 5. Parabola case. Streamflows (m^3/s) at the three sections.

TABLE 2. Parabola case: experimental convergence rates of L^1 and L^2 cell-based error norms.

	η				$\left\|\eta\vec{U}\right\|^2$			
h_ℓ	E_{L^1}	eoc_ℓ	E_{L^2}	eoc_ℓ	E_{L^1}	eoc_ℓ	E_{L^2}	eoc_ℓ
0.494	4.14E−01		2.04E−01		1.71E−00		9.49E−01	
0.248	2.58E−01	0.69	1.42E−01	0.52	1.02E−00	0.76	6.50E−01	0.55
0.124	1.47E−01	0.81	9.29E−02	0.62	5.92E−01	0.78	4.36E−01	0.57
0.062	7.58E−02	0.96	5.50E−02	0.76	3.11E−01	0.93	2.68E−01	0.70
0.032	3.02E−02	1.32	2.51E−02	1.13	1.27E−01	1.30	1.26E−01	1.09

$t = 0.00\,\text{s}$, $0.50\,\text{s}$, $1.00\,\text{s}$ and $1.50\,\text{s}$. The progress of the dam-break wave towards the outlet is characterized by a variable speed of propagation. The downwind shock initially smoothed by the numerical viscosity introduced by the 1st order solver is sharpened downstream by curvature effects, as the decreasing slope is decelerating the wave front. Also the upstream wave seems to sharpen, as evidenced by a shorter wave length at the end of the simulation. The results display some oscillations, in particular at the tail of the downstream wave, which remain always bounded and do not seem to interfere with the trailing wave. We attribute these oscillations to our treatment of the non-autonomous flux function, since they are not present in planar cases with a spatially constant metric. Figure 5 represents the time behavior of the simulated discharge at three channel cross sections located at $x^1 = 2.5\,\text{m}$, $5.0\,\text{m}$ and $7.5\,\text{m}$. Mass balance calculated a posteriori is exactly satisfied up to quadrature error.

We carried out a convergence test by using a mesh sequence starting from a coarse level characterized by $h_0 = 0.49\,\text{m}$ and 154 FV surface cells and composed by five mesh levels built by uniform refinement. Table 2 reports the L^1 and L^2-norms of the errors for the water depth and the velocity magnitude at time $t = 0.20\,\text{s}$. We assume the numerical solution calculated on the finest grid ($\ell = 5$, average mesh parameter $h_5 \approx 0.016\,\text{m}$) is the reference exact solution. First order convergence rates are attained by the L^1, L^2 error norms for both water depth and velocity.

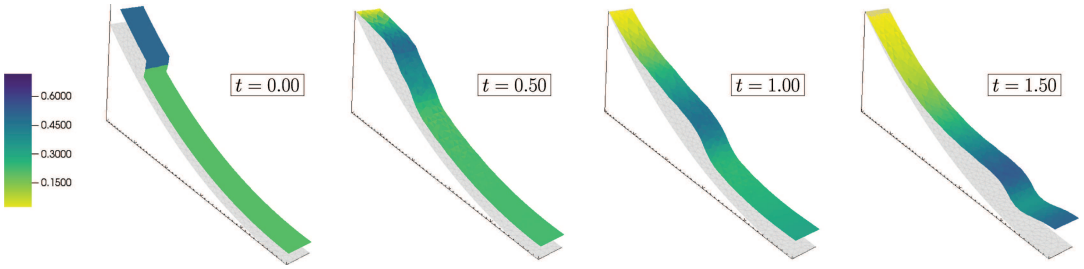

FIGURE 6. Parabola case: same as Figure 4 with active bottom friction.

We also performed a simulation where bottom friction is included by means of standard Manning's equation:

$$\frac{\mathbf{f}_{\mathcal{B}}}{\rho} = \frac{gn^2\vec{U}\left|\vec{U}\right|_{\mathcal{G}}}{\eta^{1/3}},$$

where the Manning coefficient n is equal to $0.09\,\mathrm{s/m}^{1/3}$. This friction term is incorporated into the FV code by means of a time-splitting approach. The results shown in Figure 6 clearly display a slower wave propagating downwards.

4.3. Test case 2: hyperboloid-central-bump

The following test case that presents an "almost" centrally symmetric domain is designed to verify the ability of the FV scheme to maintain symmetry on an unstructured grid. The square subset $U = [-3,3]\times[-3,3] \subset \mathbb{R}^2$ is discretized by a Delaunay triangulation with average mesh parameter $h = 0.34\,\mathrm{m}$, generating a total of 1238 FV surface cells. The nodal values are then raised using equation (4.1). The initial conditions outline a central area of radius 0.5 m with upstream water depth of 2.0 m and downstream water depth of 1.0 m, leading to an initially symmetric gravity wave. Outflow conditions are imposed on all boundaries. We use again the HLL solver.

Figure 7 shows the numerically evaluated evolution of the initial wave in terms of water depth η at times $t = 0.0\,\mathrm{s}$, $0.20\,\mathrm{s}$, $0.40\,\mathrm{s}$ and $0.60\,\mathrm{s}$. The initial wave moves downward with radial velocity vectors towards the outlet. The dynamics of the flow is such that the downstream portion of the initial dam-break wave accelerates faster than the upstream region because of the larger bottom slope. Some oscillations are created by the Riemann solver at the tail of the downstream wave, but these remain bounded and do not interfere with the trailing wave. As for the parabola case, we attribute these oscillations to our treatment of the non-autonomous fluxes. Nonetheless, the numerical results shows a rather symmetric wave pattern, demonstrating the robustness of the chosen numerical approach. This is further evidenced in Figure 8 (*left*), where the velocity vectors at $t = 0.20\,\mathrm{s}$ are shown. The radial pattern of the direction of the fluid motion is maintained everywhere in the domain and at different times, showing again that the FV scheme well captures the essence of the gravity flow. The streamflows at the three different sections, located at a radial distance from the center of 1.0 m, 1.75 m and 2.5 m are shown in Figure 8 (*right*).

For the convergence test we start from a coarse grid with average mesh parameter $h_0 = 0.56\,\mathrm{m}$ and 424 FV surface cells. The mesh sequence is obtained by uniform refinements with a total of 6 mesh levels. The reference solution is obtained at level $\ell = 5$ (average mesh parameter $h = 0.018\,\mathrm{m}$). Table 3 presents L^1 and L^2 error norms and related experimental orders of convergence for the solutions at time $t = 0.08\,\mathrm{s}$. Consistently with the previous test cases, the expected first order convergence is achieved in both norms.

4.4. Test case 3: fully 3D surface

The final test case considers a bottom surface with variable curvature. The discretization of U is obtained again with a Delaunay triangulation with average mesh parameter $h = 0.62\,\mathrm{m}$, in this case generating a total of

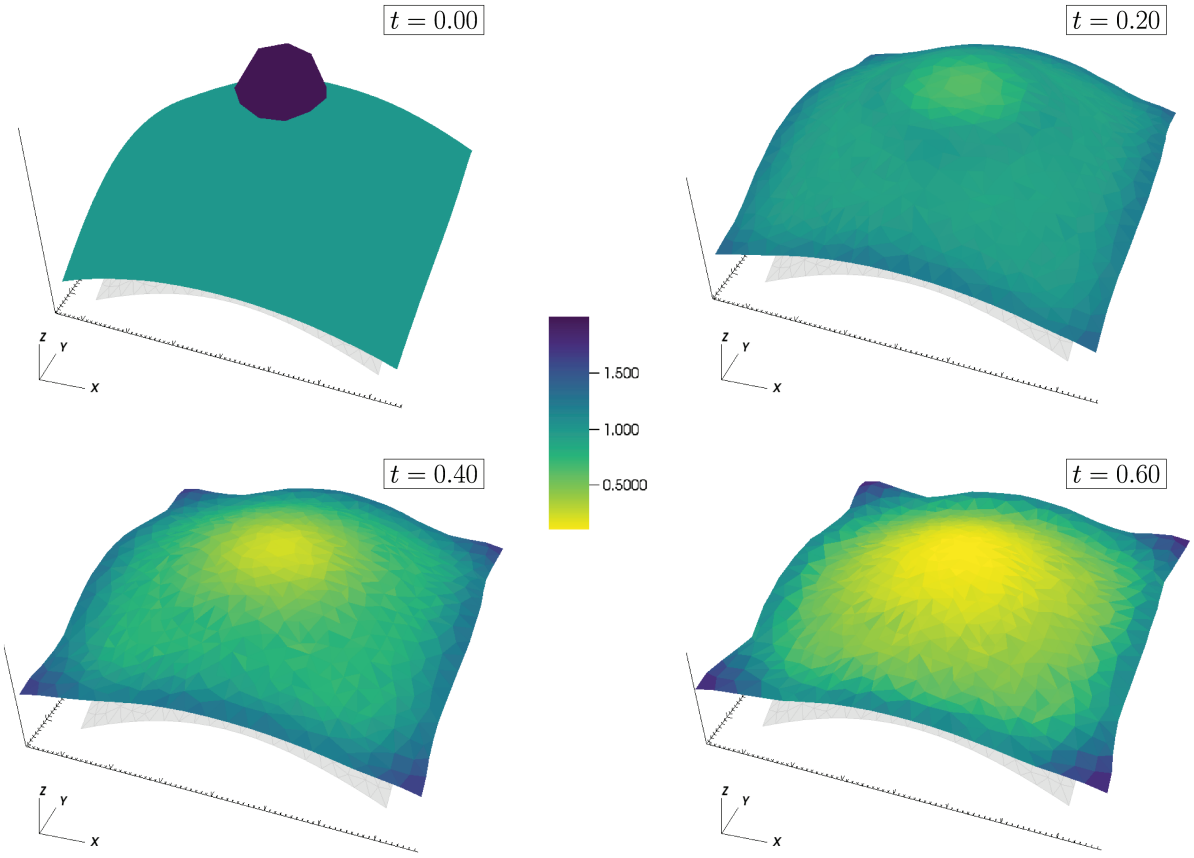

FIGURE 7. HCB: water depth at initial time ($t = 0.0\,\mathrm{s}$), and at $t = 0.20\,\mathrm{s}$, $0.40\,\mathrm{s}$, $0.60\,\mathrm{s}$.

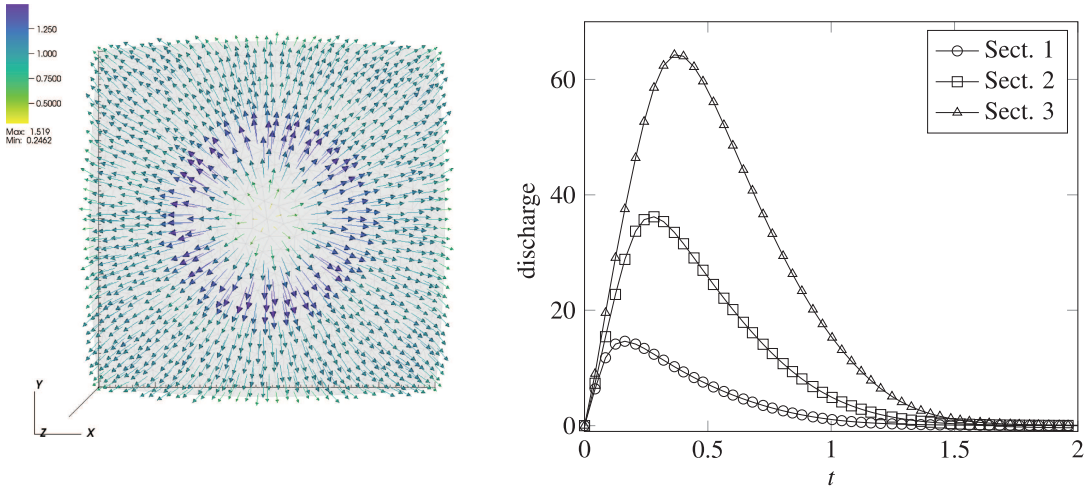

FIGURE 8. HCB: velocity vectors (m/s) at $t = 0.20\,\mathrm{s}$ and streamflows (m^3/s) at the three preselected sections.

TABLE 3. Experimental errors on cells and order of convergence for the HCB case in the L^1, L^2 norm.

	η				$\left\|\eta\vec{U}\right\|^2$			
h_ℓ	E_{L^1}	eoc_ℓ	E_{L^2}	eoc_ℓ	E_{L^1}	eoc_ℓ	E_{L^2}	eoc_ℓ
0.560	1.16E+00		3.05E−01		5.42E+00		1.32E+00	
0.281	7.20E−01	0.69	2.02E−01	0.60	2.98E+00	0.87	7.56E−01	0.81
0.140	4.03E−01	0.84	1.27E−01	0.67	1.49E+00	0.99	4.44E−01	0.77
0.070	2.13E−01	0.92	7.32E−02	0.79	8.61E−01	0.80	3.16E−01	0.49
0.035	9.54E−02	1.16	3.66E−02	1.00	3.22E−01	1.42	1.32E−01	1.26

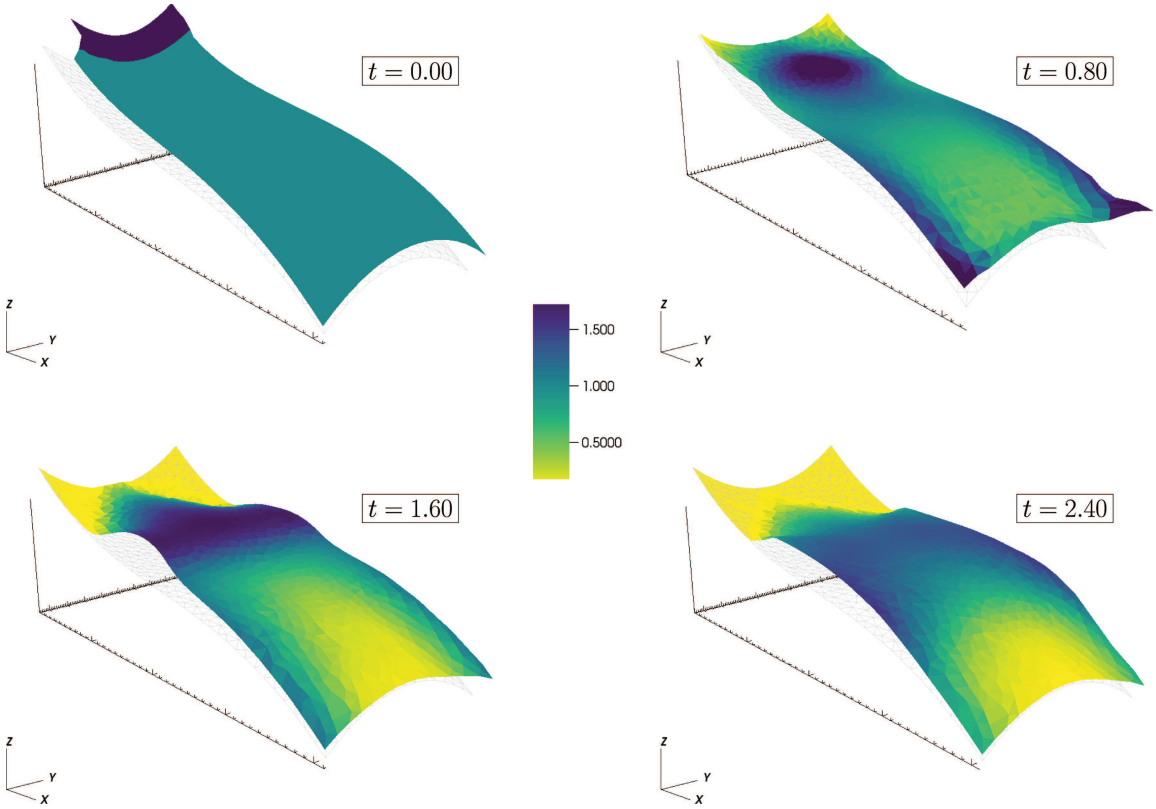

FIGURE 9. Fully 3D surface: water depth evolution of initial wave, shown both as color codes and depth elevation at initial time ($t = 0.0\,\text{s}$) and at $t = 0.80\,\text{s}$, $1.60\,\text{s}$, $2.40\,\text{s}$.

1656 FV surface cells. The initial conditions consider a uniform water depth of 2.0 m upstream of $x^1 = -8.5\,\text{m}$, and 1.0 m downstream. We would like to note that the choice of initial conditions of a 2.0 m deep reservoir avoids the singularities of the coordinate transformation by ensuring that the water depth is sufficiently shallow, so that the local normals to the bottom surface do not intersect within the fluid layer. No flow conditions are imposed in all boundaries, with an outlet located at $x^1 = 10\,\text{m}$. The approximate HLL Riemann solver is used.

Figure 9 describes the numerically evaluated water depth η at times $t = 0.0\,\text{s}$, $0.80\,\text{s}$, $1.60\,\text{s}$ and $2.40\,\text{s}$. The evolution of the profile is similar to what reported in [18]. Water accumulates within the central portion of the

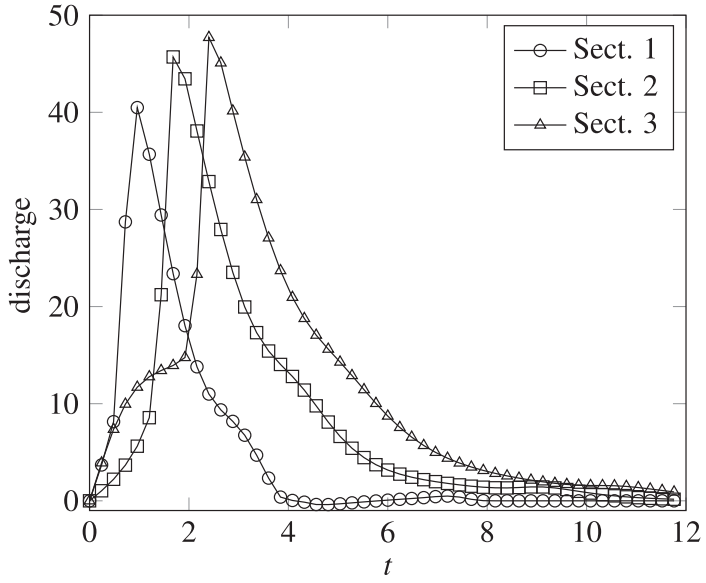

FIGURE 10. Fully 3D surface. Streamflows (m^3/s) at the three control sections.

TABLE 4. Experimental errors on cells and order of convergence for the fully 3D surface case in the L^1, L^2 norm.

	η				$\left\|\eta\vec{U}\right\|^2$			
h_ℓ	E_{L^1}	eoc_ℓ	E_{L^2}	eoc_ℓ	E_{L^1}	eoc_ℓ	E_{L^2}	eoc_ℓ
1.113	6.95E+00		8.58E−01		3.14E+01		4.19E+00	
0.564	4.15E+00	0.76	5.48E−01	0.66	1.74E+01	0.86	2.54E+00	0.74
0.284	2.36E+00	0.82	3.47E−01	0.66	9.30E+00	0.92	1.53E+00	0.73
0.142	1.22E+00	0.96	2.03E−01	0.78	4.55E+00	1.04	8.77E−01	0.81
0.071	4.97E−01	1.29	9.32E−01	1.13	1.76E+00	1.37	3.99E−01	1.14

first bowl and then disperses towards the lateral boundaries in the concave region, until it finds the impermeable lateral walls. At the end water exits from the downstream edge, where the outlet is located. Figure 10 shows streamflows at the three different sections located at $x^1 = -5.0\,\text{m}$, $0.0\,\text{m}$ and $5.0\,\text{m}$. Again, the results compare well with those obtained by [18].

The mesh sequence used to test convergence of the FV scheme starts with coarse grid with average mesh parameter $h_0 = 1.11\,\text{m}$, for a total of a 480 FV surface cells, uniformly refined 5 times to yield 6 meshes. The finest, used for the reference solution, is characterized by $h_5 = 0.036\,\text{m}$ and 491 520 FV surface triangles. The initial conditions defined on the coarsest mesh $\ell = 0$ are projected on each mesh level using the local normals taking care that the initial water volume and the location of the dam are consistently the same across the entire mesh sequence.

Table 4 reports the L^1 and L^2-error norms of the depth and of the velocity magnitude at $t = 0.20\,\text{s}$ together with the experimental order of convergence. The same behavior as for the previous test is observed, with optimal rates being reached by the water depth and the velocity field.

5. Conclusions

We have presented a novel formulation of the intrinsic shallow water equations with variable topography. The SW equations are obtained by integrating the Navier–Stokes equations along local normals defined on a local reference system anchored on the bottom surface. The resulting reduced model is written in a form intrinsic to the bottom geometry. The formulation is a second order approximation of the NS equation, is rotational invariant, maintains the lake-at-rest solution, and admits a conserved energy in case of no stresses.

The main advantage of the proposed intrinsic balance system of hyperbolic equations is that source terms contain only information related to bottom slope and curvatures, and not to the velocity field. The geometrically intrinsic description of the equations, and thus the existence of an intrinsic diverge theorem, allows a direct derivation of a Godunov finite volume discretization defined on a bottom triangulation. The geometric information of the bed surface is assumed to be available only at the triangulation nodes. Careful interpolation together with a discretized version of parallel transport is used to define approximate tangent planes on the triangle edges and barycenters. As typical of the Godunov approach, flux evaluation proceeds by approximately solving a Riemann problem on the edges. Appropriately modified midpoint quadrature rules are used to evaluate integrals over curvilinear edges and triangles.

The scheme is tested on several realistic examples showing that optimal order of convergence is obtained for smooth solutions. Mass conservation properties are verified by looking at streamflows across several control sections. The results show that the approach is accurate and robust and can be effectively used to solve hyperbolic systems on general bottom topographies.

Acknowledgements. This work was supported in part by the UniPD-SID-2016 project Approximation and discretization of PDEs on Manifolds for Environmental Modeling and the EU-H2020 ERA-PLANET Project GEOEssential "Essential Variables workflows for resource efficiency and environmental management" (ERA-PLANET no. 689443). All the three-dimensional figures were prepared using the VisIt High Performance visualization package [13].

References

[1] M. Abate and F. Tovena, Curves and Surfaces. Springer-Verlag Italia, Milano, Italy (2012).
[2] B. Andreianov and K. Sbihi, Well-posedness of general boundary-value problems for scalar conservation laws. *Trans. AMS* **367** (2015) 3763–3806.
[3] B. Andreianov, K.H. Karlsen and N.H. Risebro, On vanishing viscosity approximation of conservation laws with discontinuous flux. *Netw. Heterogen. Media* **5** (2010) 617–633.
[4] B. Andreianov, K.H. Karlsen and N.H. Risebro, A theory of l^1-dissipative solvers for scalar conservation laws with discontinuous flux. *Arch. Ratio. Mech. Anal.* **201** (2011) 27–86.
[5] E. Audusse, F. Bouchut, M. Bristeau, R. Klein and B. Perthame, A fast and stable well-balanced scheme with hydrostatic reconstruction for shallow water flows. *SIAM J. Sci. Comput.* **25** (2004) 2050–2065.
[6] E. Audusse, C. Chalons and P. Ung, A simple well-balanced and positive numerical scheme for the shallow-water system. *Commun. Math. Sci.* **13** (2015) 1317–1332.
[7] C. Berthon and C. Chalons, A fully well-balanced, positive and entropy-satisfying Godunov-type method for the shallow-water equations. *Math. Comput.* **85** (2016) 1281–1307.
[8] F. Bouchut, Nonlinear Stability of Finite Volume Methods for Hyperbolic Conservation Laws and Well-Balanced Schemes for Sources. Birkhaäuser Verlag, Basel, Switzerland (2004).
[9] F. Bouchut and S. Boyaval, A new model for shallow viscoelastic fluids. *Math. Models Methods Appl. Sci.* **23** (2013) 1479–1526.
[10] F. Bouchut and M. Westdickenberg, Gravity driven shallow water models for arbitrary topography. *Commun. Math. Sci.* **2** (2004) 359–389.
[11] F. Bouchut, A. Mangeney-Castelnau, B. Perthame and J.-P. Vilotte, A new model of Saint Venant and Savage–Hutter type for gravity driven shallow water flows. *C. R. Math. Acad. Sci. Paris* **336** (2003) 531–536.
[12] D. Bresch, Shallow-water equations and related topics, chapter 1. In: Vol. 5 of *Handbook of Differential Equations: Evolutionary Equations*, edited by C. Dafermos and M. Pokorný. North-Holland (2009) 1–104.
[13] H. Childs, E. Brugger, B. Whitlock, J. Meredith, S. Ahern, D. Pugmire, K. Biagas, M. Miller, C. Harrison, G.H. Weber, H. Krishnan, T. Fogal, A. Sanderson, C. Garth, E.W. Bethel, D. Camp, O. Rübel, M. Durant, J.M. Favre and P. Navrátil, VisIt: an end-user tool for visualizing and analyzing very large data. In: High Performance Visualization – Enabling Extreme-Scale Scientific Insight (2012) 357–372.
[14] A. Decoene, L. Bonaventura, E. Miglio and F. Saleri, Asymptotic derivation of the section-averaged shallow water equations for natural river hydraulics. *Math. Models Methods Appl. Sci.* **19** (2009) 387–417.

[15] O. Delestre, C. Lucas, P.-A. Ksinant, F. Darboux, C. Laguerre, T.N.T. Vo, F. James and S. Cordier. SWASHES: a compilation of shallow water analytic solutions for hydraulic and environmental studies. *Int. J. Numer. Methods Fluids* **72** (2013) 269–300.

[16] M.P. Do Carmo, Differential Geometry of Curves and Surfaces. Prentice-Hall, Englewood Cliffs, New Jersey (1976).

[17] G. Dziuk and C.M. Elliott, Finite element methods for surfaces PDEs. *Acta Numer.* **22** (2013) 289–396.

[18] I. Fent, M. Putti, C. Gregoretti and S. Lanzoni, Modeling shallow water flows on general terrains. *Adv. Water Resour.* **121** (2018) 316–332.

[19] E.D. Fernández-Nieto, F. Bouchut, D. Bresch, M.J. Castro Díaz and A. Mangeney-Castelnau, A new Savage–Hutter type model for submarine avalanches and generated tsunami. *J. Comput. Phys.* **227** (2008) 7720–7754.

[20] K. Georg and J. Tausch, Some error estimates for the numerical approximation of surface integrals. *Math. Comput.* **62** (1994) 755–763.

[21] J.M.N.T. Gray, M. Wieland and K. Hutter, Gravity-driven free surface flow of granular avalanches over complex basal topography. *Philos. Trans. R. Soc. A* **455** (1999) 1841–1874.

[22] A. Harten, P.D. Lax and B.V. Leer, On upstream differencing and Godunov-type schemes for hyperbolic conservation laws. *SIAM Rev.* **25** (1983) 35–61.

[23] R.L. Higdon, Numerical modelling of ocean circulation. *Acta Numer.* **15** (2006) 385–470.

[24] J.R. Holton, An Introduction to Dynamic Meteorology. Elsevier Academic Press, Burlington, MA (2004).

[25] R.M. Iverson and D.L. George, A depth-averaged debris-flow model that includes the effects of evolving dilatancy. I. Physical basis. *Proc. R. Soc. London* **470** (2014) 20130819.

[26] S. Lanzoni, A. Siviglia, A. Frascati and G. Seminara, Long waves in erodible channels and morphodynamic influence. *Water Resour. Res.* **42** (2006) W06D17.

[27] L. Moretti, K. Allstadt, A. Mangeney-Castelnau, Y. Capdeville, E. Stutzmann and F. Bouchut, Numerical modeling of the Mount Meager landslide constrained by its force history derived from seismic data. *J. Geophys. Res.* **120** (2015) 2579–2599.

[28] J.-M. Morvan, Generalized Curvatures. In: Vol. 2 of *Geometry and Computing*. Springer Science & Business Media, Berlin, Heidelberg (2008).

[29] P. Nevalainen, I. Jambor, J. Pohjankukka, J. Heikkonen and T. Pahikkala, Triangular curvature approximation of surfaces – filtering the spurious mode. In: *6th International Conference on Pattern Recognition Applications and Methods*. SCITEPRESS – Science and Technology Publications (2017) 684–692.

[30] S. Nigam and V. Agrawal, A Review: Curvature approximation on triangular meshes. *Int. J. Eng. Sci. Innov. Technol. (IJESIT)* **2** (2013) 330–339.

[31] M. Pelanti, F. Bouchut and A. Mangeney-Castelnau, A Roe-type scheme for two-phase shallow granular flows over variable topography. *ESAIM: M2AN* **42** (2008) 851–885.

[32] J.A. Rossmanith, D.S. Bale and R.J. LeVeque, A wave propagation algorithm for hyperbolic systems on curved manifolds. *J. Comput. Phys.* **199** (2004) 631–662.

[33] S.B. Savage and K. Hutter, The motion of a finite mass of granular material down a rough incline. *J. Fluid Mech.* **199** (1989) 177–215.

[34] S.B. Savage and K. Hutter, The dynamics of avalanches of granular materials from initiation to runout. Part I: Analysis. *Acta Mech.* **86** (1991) 201–223.

[35] T. Song, A. Main, G. Scovazzi and M. Ricchiuto, The shifted boundary method for hyperbolic systems: embedded domain computations of linear waves and shallow water flows. *J. Comput. Phys.* **369** (2018) 45–79.

[36] E. Toro, Shock-Capturing Methods for Free-Surface Shallow Flows. John Wiley (2001).

[37] E. Toro, M. Spruce and W. Speares, Restoration of the contact surface in the Harten–Lax–van Leer Riemann solver. *Shock Waves* **4** (1994) 25–34.

[38] G. Zolezzi and G. Seminara, Downstream and upstream influence in river meandering. Part 1. General theory and application to overdeepening. *J. Fluid Mech.* **438** (2001) 183–211.